

<b>REPORT DOCUMENTATION PAGE</b>					Form Approved OMB No. 0704-0188							
<p>The public reporting burden for this collection of information is estimated to average 1 hour per response, including the time for reviewing instructions, searching existing data sources, gathering and maintaining the data needed, and completing and reviewing the collection of information. Send comments regarding this burden estimate or any other aspect of this collection of information, including suggestions for reducing the burden, to Department of Defense, Washington Headquarters Services, Directorate for Information Operations and Reports (0704-0188), 1215 Jefferson Davis Highway, Suite 1204, Arlington, VA 22202-4302. Respondents should be aware that notwithstanding any other provision of law, no person shall be subject to any penalty for failing to comply with a collection of information if it does not display a currently valid OMB control number.</p> <p><b>PLEASE DO NOT RETURN YOUR FORM TO THE ABOVE ADDRESS.</b></p>												
<b>1. REPORT DATE (DD-MM-YYYY)</b> 31-03-2016		<b>2. REPORT TYPE</b> FINAL		<b>3. DATES COVERED (From - To)</b> 02/01/2010-12/31/2015								
<b>4. TITLE AND SUBTITLE</b> PECASE: Multi-spectral Photon Detection in Polymer/Nanoparticle Composites-Toward IR Photodectors and Solar Cells Applicable to Unmanned Vehicles				<b>5a. CONTRACT NUMBER</b>								
				<b>5b. GRANT NUMBER</b> N00014-10-1-0481								
				<b>5c. PROGRAM ELEMENT NUMBER</b>								
<b>6. AUTHOR(S)</b> Adrienne Stiff-Roberts				<b>5d. PROJECT NUMBER</b> 15PR09272-00								
				<b>5e. TASK NUMBER</b>								
				<b>5f. WORK UNIT NUMBER</b>								
<b>7. PERFORMING ORGANIZATION NAME(S) AND ADDRESS(ES)</b> Duke University Office of Research Support 2200 West Main Street Ste 710 Durham, NC 27705-4677				<b>8. PERFORMING ORGANIZATION REPORT NUMBER</b> 1								
<b>9. SPONSORING/MONITORING AGENCY NAME(S) AND ADDRESS(ES)</b> Duke University Office of Sponsored Programs 2200 West Main Street Ste 300 Durham, NC 27705-467				<b>10. SPONSOR/MONITOR'S ACRONYM(S)</b>								
				<b>11. SPONSOR/MONITOR'S REPORT NUMBER(S)</b> 313-0131								
<b>12. DISTRIBUTION/AVAILABILITY STATEMENT</b> No restrictions on who can read or have access to the report												
<b>13. SUPPLEMENTARY NOTES</b>												
<b>14. ABSTRACT</b> The overall objective of this work was to enable multi-spectral photon detection using hybrid nanocomposites. The core contribution of this work was the development of emulsion-based, resonant infrared matrix-assisted pulsed laser evaporation (RIR-MAPLE) for the deposition of hybrid nanocomposite devices. Significant contributions from this endeavor include demonstrating the unique morphology of hybrid nanocomposites deposited by RIR-MAPLE; demonstrating hybrid nanocomposite infrared photodetectors and solar cells deposited by RIR-MAPLE, and developing a simulation tool for optoelectronic device performance that accounts for RIR-MAPLE film properties.												
<b>15. SUBJECT TERMS</b> Hybrid nanocomposites, MAPLE, RIR-MAPLE, intraband absorption, mid-IR photodetectors, organic solar cells, Dynamic Monte Carlo simulation												
<b>16. SECURITY CLASSIFICATION OF:</b> <table border="1" style="width: 100%; border-collapse: collapse;"> <tr> <td style="width: 33%; padding: 2px;"><b>a. REPORT</b></td> <td style="width: 33%; padding: 2px;"><b>b. ABSTRACT</b></td> <td style="width: 33%; padding: 2px;"><b>c. THIS PAGE</b></td> </tr> <tr> <td style="text-align: center; padding: 2px;">N/A</td> <td style="text-align: center; padding: 2px;">N/A</td> <td style="text-align: center; padding: 2px;">N/A</td> </tr> </table>			<b>a. REPORT</b>	<b>b. ABSTRACT</b>	<b>c. THIS PAGE</b>	N/A	N/A	N/A	<b>17. LIMITATION OF ABSTRACT</b>		<b>18. NUMBER OF PAGES</b> 49	
<b>a. REPORT</b>	<b>b. ABSTRACT</b>	<b>c. THIS PAGE</b>										
N/A	N/A	N/A										
			<b>19a. NAME OF RESPONSIBLE PERSON</b> Adrienne Stiff-Roberts									
			<b>19b. TELEPHONE NUMBER (Include area code)</b> 919-660-5560									

## **Final Technical Report**

**Project:** ONR PECASE

**Contract Number:** N00014-10-1-0481

**AFOSR PM:** Dr. Kenny Lipkowitz

**Report Date:** March 31, 2016 (For the period of Feb. 1, 2010 to December 31, 2015)

**Title:** Multi-spectral Photon Detection in Polymer/Nanoparticle Composites – Toward IR Photodetectors and Solar Cells Applicable to Unmanned Vehicles (PECASE)

**PI:** Prof. Adrienne Stiff-Roberts, Duke University

## TABLE OF CONTENTS

Section	Page
LIST OF FIGURES.....	iii
LIST OF TABLES.....	vi
1.0 SUMMARY.....	1
2.0 INTRODUCTION.....	1
3.0 METHODS, ASSUMPTIONS, AND PROCEDURES .....	4
4.0 RESULTS AND DISCUSSION.....	5
4.1 Unique Morphology of Hybrid Nanocomposites Deposited by RIR-MAPLE....	5
4.2 Multi-spectral, Hybrid Nanocomposite Infrared Photodetectors Deposited by RIR-MAPLE .....	14
4.3 Organic and Hybrid Nanocomposite Solar Cells Deposited by RIR-MAPLE.	23
4.4 Simulation Tool for Optoelectronic Device Performance in Thin Films Deposited by RIR-MAPLE.....	33
5.0 CONCLUSIONS.....	38
APPENDIX A – LIST OF PUBLICATIONS.....	40



## LIST OF FIGURES

Figure 1.	Schematic diagram of RIR-MAPLE system. ....	2
Figure 2.	TOF photocurrent transients of spin-cast, drop-cast, and RIR-MAPLE-deposited MEH-PPV films at 30°C and an applied field of 510 (V/cm) <sup>1/2</sup> . The inset shows the same transients on a log-log scale. ....	6
Figure 3.	Hole drift mobility for spin-cast, drop-cast, and RIR-MAPLE-deposited MEH-PPV thin films as a function of the square root of the electric field for multiple measurement temperatures. ....	7
Figure 4.	Two-dimensional GIWAXS measurements of a representative RIR-MAPLE-deposited P3HT thin film compared with drop-cast and spin-cast P3HT thin films. RIR-MAPLE parameters are: 7 cm TS distance; with SDS; annealed at 140 C for 30 minutes. ....	8
Figure 5.	(a) Due to deep laser absorption and excitonic dissociation in the nanocomposite, a volume of charge is photogenerated and the TOF transit time cannot be accurately extracted from the resultant current transient. (b) The modified TOF method uses a layered structure that consists of a pure MEH-PPV laser absorbing layer and a MEH-PPV-CdSe CQD transport layer. The transit time of the pure MEH-PPV layer is subtracted from the transit time of the entire heterostructure to find the transit time of the nanocomposite layer. ....	9
Figure 6.	Hole drift mobility vs. temperature and electric field for nanocomposite thin films with different MEH-PPV:CdSe CQD ratios. ....	10
Figure 7.	TEM images of PCPDTBT/TOPO-capped CdSe hybrid nanocomposite films deposited by spin-casting using (a)(d) chlorobenzene, (b)(e) dichlorobenzene, (c)(f) trichlorobenzene as the solvent and deposited by RIR-MAPLE using (g)(j) chlorobenzene, (h)(k) dichlorobenzene, (i)(l) trichlorobenzene as the primary solvent. The scale bars are labeled on the images. ....	13
Figure 8.	TEM images of PCPDTBT/pyridine-capped CdSe hybrid nanocomposite films deposited by (a) (b)(c) spin-casting using trichlorobenzene as the solvent and deposited by (d)(e)(f) RIR-MAPLE using trichlorobenzene as the primary solvent. The scale bars are labeled in the images. ....	14
Figure 9.	Schematic representation of finite spherical potential for CdSe/surface ligand/MEH-CN-PPV nanocomposite. ....	15
Figure 10.	Comparison of normalized calculated absorption coefficient and measured absorbance. ....	16
Figure 11.	Comparison of normalized absorption coefficient for various ligand materials. ....	16
Figure 12.	Comparison of absorption coefficient for various ligand materials. ....	17
Figure 13.	The preparation and observed morphology of four different hybrid nanocomposite samples designed to investigate CQD dispersion. ....	19



Figure 14. TEM images of nanocomposites: (a) Sample 1 and (b) Sample 4; (c) magnified image of Sample 4 demonstrating dispersed CdSe CQDs within the polymer matrix; and (d) OsO <sub>4</sub> -stained Sample 4 demonstrating location of MEH-CN-PPV and PAEM. ....	19
Figure 15. TRPL spectra (excited at 405 nm, 1.5 $\mu$ W, measured in 530-555 nm) of the four nanocomposite samples in solid state and a reference MEH-CN-PPV film. The measured TRPL decay lifetimes are shown in the inset. ....	20
Figure 16. Schematic and TEM images of CdSe CQDs/MEH-CN-PPV blend and in-situ polymerized CdSe CQDs/MEH-CN-PPV nanocomposites. ....	21
Figure 17. Spectral responsivities of in-situ polymerized CdSe/MEH-CN-PPV hybrid nanocomposite photodetector (4% AEM) in the a) visible region (300 nm to 700 nm); (b) the IR region (2.5 $\mu$ m to 4 $\mu$ m); and c) the IR region (4 $\mu$ m to 5.5 $\mu$ m). The UV-Vis absorption spectrum for the same nanocomposite material is also shown. ....	22
Figure 18. J-V curves of PCPDTBT:PC71BM BHJ OSCs (1:1) deposited by RIR-MAPLE using different SDS weight concentration prepared in DI water. ....	23
Figure 19. (a) J-V characteristics of PCPDTBT:PC71BM (1:1) BHJ OSCs fabricated by simultaneous (red) and sequential (black) deposition modes. The inset table is calculated performance parameters. (b) Stacked UV-Vis-NIR absorbance spectra of blended PCPDTBT:PC71BM (1:1) films deposited by simultaneous (red) and sequential (black) deposition modes. ....	24
Figure 20. (a) Stacked UV-Vis-NIR absorbance spectra of PCPDTBT:PC71BM blended films with different ratios deposited by sequential deposition mode. The attribution of the peaks are highlighted by arrow marks. (b) The J-V curves of PCPDTBT:PC71BM BHJ OSCs deposited by sequential deposition mode. ....	25
Figure 21. Average photocurrent density versus applied bias for each of the five RIR-MAPLE target volume ratios: 1:3, 1:2, 1:1, 2:1, and 3:1. Each curve is the average of six different 9 mm <sup>2</sup> devices. ....	26
Figure 22. Average J-V characteristics of the 2nd ratio study to determine the true optimum RIR-MAPLE target ratio of P3HT:PC61BM in a BHJ OPV device. Each curve is the average of six different 9 mm <sup>2</sup> devices. The work was motivated by knowledge of the optimum ratio of P3HT:PCBM in spin-cast films, which is slightly larger than unity. ....	27
Figure 23. AFM height images of PCPDTBT films deposited from chlorobenzene, 1,2-dichlorobenzene, and 1,2,4-trichlorobenzene. ....	29
Figure 24. The J-V curves of PCPDTBT:PC71BM BHJ OSCs (1:1.5) deposited by RIR-MAPLE using different primary solvents for PCPDTBT target emulsion. ....	29
Figure 25. AFM height images of P3HT:PCBM films deposited from the six primary solvents. ....	30
Figure 26. The J-V curves of P3HT:PC61BM BHJ OSCs (1:1.5) deposited by RIR-MAPLE using different primary solvents for P3HT target emulsion. ....	30

Figure 27. (a) J-V curve of PCPDTBT-pyridine CdSe hybrid organic solar cell fabricated by RIR-MAPLE; and (b) EQE spectra of the corresponding solar cells with different CdSe loading. ....	31
Figure 28. Energy band diagram for PCPDTBT-PC71BM organic solar cells fabricated by RIR-MAPLE with different tandem structures. ....	32
Figure 29. J-V curves of PCPDTBT-PC71BM organic solar cells fabricated by RIR-MAPLE with different tandem structures. ....	33
Figure 30. Zeiss LSM 510 confocal microscope images for RIR-MAPLE P3HT:PC61BM BHJs of different ratios: 1:1, 2:1, and 3:1 showing the structural changes in features on two different size scales: (1) 36 x 36 $\mu$ m; (2) 100 x 100 $\mu$ m. The red regions represent the polymer, while the black regions represent the small molecule. ....	34
Figure 31. GI-WAXS images of 2D scattering intensity for RIR-MAPLE P3HT:PC61BM BHJs of different ratios. Images for RIR-MAPLE P3HT- and PC61BM-alone samples are included for comparison. ....	35
Figure 32. 1D GI-WAXS scattering profiles obtained from Figure 3 by integration along the (a) out-of-plane (OOP) and (b) in-plane (IP) directions, and normalized to the P3HT (100) peak around $q=0.3\text{\AA}^{-1}$ . ....	35
Figure 33. Schematic diagrams of the different P3HT:PC61BM OPV heterostructures fabricated using RIR-MAPLE. ....	36
Figure 34. Atomic compositions of S 2p (squares) and C 1s (stars) peaks for P3HT:PC61BM BHJ (black lines) and graded (red lines) active regions with increasing etching times to provide a compositional depth profile of the films. ....	37
Figure 35. Simulated EQE spectra using microscale DMC model comparing different P3HT:PC61BM active region structures. ....	37
Figure 36. (a) Measured EQE spectra and (b) Jsc from measured EQE spectra, J-V data, and simulated EQE for the three active region structures of P3HT:PC61BM OPVs: BHJ, bilayer, and graded. ....	38



## LIST OF TABLES

Table 1.	The disorder model parameters for spin-cast, drop-cast, and RIR-MAPLE-deposited MEH-PPV thin films.....	8
Table 2.	The BGDM and CDM energy disorder parameters, BGDM positional disorder parameters, and CDM hopping distances of MEH-PPV-CdSe CQD thin films with different MEH-PPV:CdSe ratios. ....	10
Table 3.	Model parameters for surface ligand materials. ....	16
Table 4.	Performance of PCPDTBT:PC 71BM BHJ OSCs with different ratios fabricated by RIR-MAPLE using sequential deposition mode. The ratio of the two materials is indicated in parentheses (polymer: small molecule). All results were determined by averaging six devices. ....	26
Table 5.	OPV metrics for the P3HT:PCBM BHJ ratio study. ....	27
Table 6.	OPV metrics for the P3HT:PC61BM BHJ ratio study near 1:1. ....	28
Table 7.	Performance of PCPDTBT:PC 71BM BHJ OSCs (1:1.5) desposited by RIR-MAPLE using different primary solvents for PCPDTBT target emulsion. The results are averaged by six devices. ....	29
Table 8.	Performance of P3HT:PC 61BM BHJ OSCs (1:1.5) desposited by RIR-MAPLE using different primary solvents for P3HT target emulsion. The results are averaged by six devices.....	31
Table 9.	Summary of photovoltaic performance under one sun AM 1.5 G illumination for PCPDTBT- pyridine CdSe hybrid organic solar cells fabricated by RIR-MAPLE with different CdSe loading. ....	32
Table 10.	Summary of photovoltaic performance under one sun AM 1.5 G illumination for tandem and ternary organic solar cells fabricated by RIR-MAPLE. ....	33



## 1.0 SUMMARY

The overall objective of this work was to enable multi-spectral photon detection using hybrid nanocomposites of polymers and colloidal quantum dots (CQDs). Such multi-spectral photodetection was evaluated in the context of intraband, infrared photodetector and solar cell device applications. One of the primary challenges to using hybrid nanocomposites for such optoelectronic devices is the solvent-induced aggregation of CQDs within polymer matrices that reduces the interfacial area of the polymer matrix and CQDs upon which the device operation depends. The core contribution of this work was to address this challenge with the development of emulsion-based, resonant infrared matrix-assisted pulsed laser evaporation (RIR-MAPLE) for the deposition of hybrid nanocomposite devices. Emulsion-based, RIR-MAPLE is a distinctive processing approach for organic-based thin films that challenges the prevailing paradigm of solution-based film synthesis in three important ways: i) it is vacuum-based, ii) film deposition occurs from a laser-induced material plume, and iii) the target material is a frozen emulsion. As such, emulsion-based RIR-MAPLE provides a new framework for investigating the formation and morphology of organic-based thin films, especially hybrid nanocomposites comprising CQDs embedded in a polymer matrix.

Given this enabling technology, the material and device properties of polymeric, bulk heterojunction, and hybrid nanocomposite thin films have been investigated in order to understand the process-structure-property relationships resulting from emulsion-based RIR-MAPLE. Significant contributions from this endeavor fall into four topical areas: i) unique morphology of hybrid nanocomposites deposited by RIR-MAPLE, ii) multi-spectral, hybrid nanocomposite infrared photodetectors deposited by RIR-MAPLE, iii) organic and hybrid nanocomposite solar cells deposited by RIR-MAPLE, and iv) simulation tools for optoelectronic device performance in thin films deposited by RIR-MAPLE.

## 2.0 INTRODUCTION

In 1982, polymer deposition using pulsed laser deposition (PLD) was first demonstrated. In PLD, pure solid polymer is used as the target for ultraviolet (UV) laser ablation under vacuum. The drawback of this technique is that conducting polymers cannot be deposited due to photochemical and structural degradation resulting from direct absorption of high energy from a UV laser (typically, 248 nm KrF excimer UV laser). To minimize the degradation of the polymer, a variation of PLD, called matrix-assisted pulsed laser evaporation (MAPLE), was developed. In MAPLE deposition, the target polymer is dissolved into a volatile solvent (the host matrix) and then frozen into a solid target by liquid nitrogen. Ideally, only the host solvent absorbs the energy from the UV laser and evaporates. The remaining solute polymer is ejected from the target and deposited onto the substrate. Because the solvent evaporates as the gas phase due to the absorption of laser energy, direct solvent exposure on the substrate is limited. Although advantageous over traditional PLD, this UV-MAPLE deposition can still result in degradation of the polymer, which is especially problematic for optoelectronic applications. An alternative approach is to minimize polymer degradation by tuning an infrared laser to the vibrational energy mode of a specific bond that exists in the solvent but not in the target polymer, known as resonant infrared, matrix-assisted pulsed laser evaporation (RIR-MAPLE). This



approach was first realized using a free electron laser to tune the wavelength according to the choice of solvent. In 2008, a variation of the RIR-MAPLE technique that uses an emulsion-based target matrix was introduced by the PI and is shown in the schematic diagram of **Figure 1**. In emulsion-based RIR-MAPLE, instead of using pure volatile solvent as the frozen matrix, a frozen emulsion containing uniformly mixed solvent and water is used as the matrix. An Er:YAG laser (2.94  $\mu\text{m}$ ), which is resonant only with hydroxyl bonds (O-H) in the emulsion (primarily from water), serves as the ablating laser. Considering the high absorbance of water ice at the Er:YAG laser energy, as well as the low energy of the IR source, the degradation of chemical bonds and molecular weight in polymers is practically eliminated. Thus, emulsion-based RIR-MAPLE essentially decouples the absorption of laser energy from the guest material system, which provides wide flexibility in the choice of organic solvents, polymer matrices, and CQD nanoparticles for use in hybrid nanocomposites.

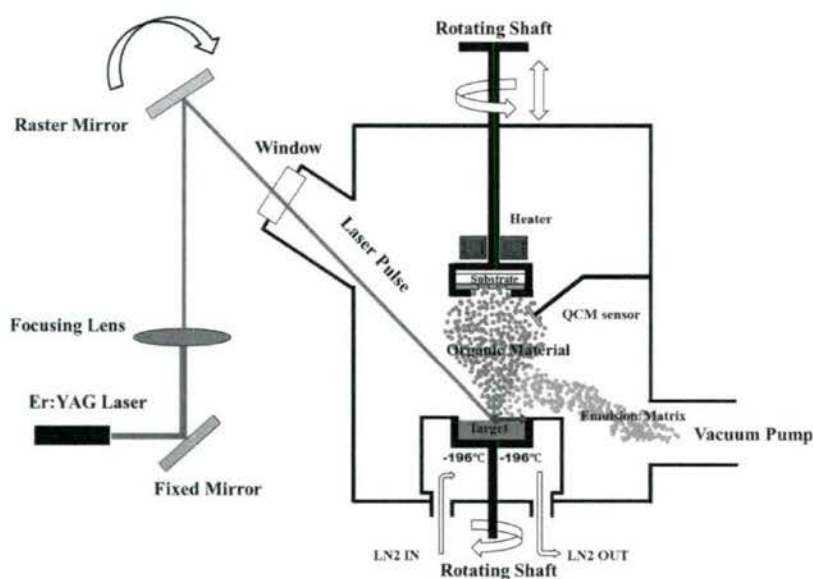


Figure 1. Schematic diagram of RIR-MAPLE system.

An important contribution from this research program is the demonstration that emulsion-based RIR-MAPLE enables unique morphologies in both polymeric and hybrid nanocomposite thin films that could address two fundamental, materials challenges to multi-spectral photon detectors using hybrid nanocomposites. First, one of the most significant limitations to using conjugated polymers (as active regions or matrices) in optoelectronic devices is the carrier mobility, which is intimately related to polymer chain crystallinity and orientation. Interchain hopping conduction is a primary charge transport mechanism in conjugated polymer thin films, thus the carrier mobility is substantially enhanced or degraded based on the deposition technique used and the resulting internal morphology of polymer thin films. Second, the chemical synthesis of CQDs involves the attachment of long organic surface ligands in order to quench the growth of the nanoparticles and prevent agglomeration; however, these ligands also impede charge transport. Therefore, it is beneficial to exchange longer surface ligands to shorter ones for optoelectronic devices. One disadvantage of these shorter ligands is the resulting



aggregation of CQDs that reduces the interfacial area between the CQDs and polymer, leading to poor dispersion of nanoparticles within a polymer matrix. Such aggregation, which also occurs due to solvent evaporation in solution-based processing, can change the size-dependent optical properties of the CQDs.

A second important contribution from this work is that emulsion-based RIR-MAPLE has been used to process hybrid nanocomposite thin films for room-temperature, multi-spectral infrared photodetectors using intraband transitions. Mid-infrared (mid-IR) photodetection is vital for applications spanning the fields of medicine, atmospheric science, astronomy, and surveillance. Hybrid nanocomposites could be especially useful for room-temperature mid-IR photodetection due to low dark current densities and quantum confinement effects in CQDs. To date, many of the IR photodetector devices that have been reported using CQDs or nanocomposite thin films have demonstrated detection in the near-IR (1-3  $\mu\text{m}$ ) corresponding to the bandgap energy of the CQD. These devices demonstrate a Type-I band lineup and rely on bipolar, interband transitions in the CQD, and photoconduction is accomplished through hole transport in the polymer and/or hopping electron conduction via the CQDs. This research demonstrated, for the first time, infrared detection in the mid-IR (3-5  $\mu\text{m}$ ), at room temperature, through the use of intraband transitions in the conduction band of the CQD embedded in a higher bandgap polymer matrix. In this case, the conjugated polymer material behaves similarly to an inorganic semiconductor material in that bands of allowed energy states are separated by a forbidden energy gap. The large bandgap and small electron affinity of the conjugated polymer provide a potential offset for the embedded CQDs giving rise to quantized energy states that are occupied by free carriers that can be promoted out of the CQD and transported via the polymer to register as a photocurrent. Therefore, the development of hybrid nanocomposite, mid-IR photodetectors that operate based on intraband transitions could constitute an important new technology for IR imaging.

Third, this research program demonstrated that organic and hybrid nanocomposite solar cells deposited by emulsion-based RIR-MAPLE could benefit from this novel deposition technique. Inorganic nanoparticles (which serve as electron acceptors) can sensitize organic solar cells to different regions of the solar spectrum. As a result, tandem solar cell junctions comprising hybrid nanocomposites with different CQD acceptors could increase the power conversion efficiency of organic-based solar cells. Traditionally, hybrid nanocomposite active regions, comprising bulk heterojunctions of CQDs embedded in polymer matrices, have been deposited using spin-casting; however, CQD aggregation within the polymer matrix is especially detrimental to achieving high power conversion efficiency due to reduced exciton dissociation. The unique hybrid nanocomposite morphology enabled by RIR-MAPLE deposition could help address this fundamental challenge.

Finally, because thin films deposited by RIR-MAPLE have fundamentally different material properties that are independent of the solvent used, a simulation tool that can determine optoelectronic device performance in these RIR-MAPLE thin films was developed in this research program. Such a simulation tool could help explore both theoretical limits and design parameters to help improve optoelectronic device performance, especially for organic-based solar cells. We developed an in-house simulation tool that determines the photocurrent for organic-based optoelectronic devices, specifically organic-based solar cells or photodetectors. This simulator is unique



because it accounts for the polymer and hybrid nanocomposite film morphologies achieved using emulsion-based RIR-MAPLE deposition by including experimentally-determined materials parameters directly into the simulation. This tool will be an integral component of advancing multi-spectral photodetection in hybrid nanocomposites.

### 3.0 METHODS, ASSUMPTIONS, AND PROCEDURES

In this work, the following organic-based material systems have been investigated: MEH-PPV:CdSe CQDs, P3HT:PC<sub>61</sub>BM, P3HT:CdSe CQDs, and PCPDTBT:PC<sub>71</sub>BM. The unique film formation mechanism and resulting film morphology of blended films, like BHJs, results from the sequential deposition mode used during RIR-MAPLE. In the sequential deposition mode, a separate emulsion is prepared for each component material (e.g. polymer and small molecule) and used to form a single, partitioned target. During film deposition, the target rotates and the laser rasters between the center and edge of the target. For each laser pulse (90  $\mu$ s pulse width), emulsified particles comprising clusters of polymer or small molecules (depending on the target partition exposed to the laser) are transferred from the target to the substrate as the continuous water phase of the emulsion is evaporated by the absorption of the laser energy. Thus, the deposited film is formed over time by the random distribution of these transferred clusters across the substrate. As a result, the constituent emulsion fraction of the target determines the composition, or blend ratio, of the deposited film. It is important to note an inherent, practical challenge faced during the course of this research is that the RIR-MAPLE system is not integrated with a glove box. Therefore, some device degradation due to atmospheric exposure cannot be avoided during the device fabrication process. An important assumption about the impact of this work is that the measured device performance reported in this document should increase by integrating a glove box with the deposition system.

Another integral component of this research program has been the development of a semi-empirical Dynamic Monte Carlo (DMC) model to simulate the external quantum efficiency in organic solar cells featuring different materials properties resulting from RIR-MAPLE deposition. The calculated output from the model includes the spectral external quantum efficiency and the short-circuit current density ( $J_{sc}$ ). The initial simulation tool has been developed in the context of OPV solar cells using bulk heterojunctions (BHJs) of P3HT and PCBM. In this way, the model results can be compared to readily available experimental data. The current simulation tool consists of three parts: i) an algorithm to generate the BHJ morphologies, ii) a transfer matrix calculation to determine the exciton generation rate and spatial distribution, and iii) a Dynamic Monte Carlo model to simulate charge transport within the organic solar cell.

The first part of the simulation tool generates random BHJ morphologies using the Ising Model and Kawasaki spin dynamics governed by the Metropolis Algorithm Monte Carlo. The Metropolis algorithm is primarily used to simulate how systems in an excited state relax towards equilibrium. In the case of morphology generation, as the energy of the system lowers and heads towards "equilibrium", larger grain sizes form and the disorder of the system is lowered. One way of controlling the morphologies generated by this simulation is by changing the runtime of the simulation.



The second part of the simulation tool calculates the exciton generation rate by treating the solar cell as a lossy microcavity and using the transfer matrix method to determine the optical field intensity as a function of wavelength and distance from the reflective cathode. The interfaces between the layers of the solar cell are assumed to be optically flat and the materials are assumed to be isotropic with complex indices of refraction. The incident solar radiation field is directed along the surface normal and has magnitude derived from the AM1.5 G solar spectrum. According to this calculated, z-dependent exciton generation rate, excitons are located randomly along the cross-sectional area of the simulated solar cell within the final simulation module.

The third part of the simulation tool is the Dynamic Monte Carlo (DMC) model used to track exciton and charge transport within the simulated organic solar cell using the First Reaction Method (FRM). In FRM, the probabilities of the possible actions are generated for a particle once that particle has executed a previous action. Excitons, holes, and electrons are tracked through a lattice of dimensions 100 x 100 x 60. The lattice constant,  $a$ , of the system determines the size of each lattice position. Energy disorder is simulated by setting each lattice position to have a random energy distributed as a Gaussian. The energy of each lattice position is then modified by the work function difference of the contacts which is 0.5 eV for aluminum-ITO. Coulombic interactions among charge carriers also modify the energy at each lattice point up to six lattice points away. Excitons can move (modeled by Förster energy transfer), dissociate, or recombine. A separated charge carrier can move (modeled by Miller-Abrahams hopping), recombine, or be collected at contacts. Charge carriers are collected at the contacts, which are located at  $z = 0$  and  $z = 60$ . The dynamics within the system are on the scale of nanoseconds and picoseconds, so the DMC model was run for at least 10  $\mu$ s, which is enough time for the system to reach a steady state. Five numbers are tracked as the charge transport model runs: number of carriers in the cell, total number of holes collected, total number of electrons collected, total number of excitons created, and total number of excitons dissociated. Once steady state is achieved, the following efficiencies are determined: exciton dissociation efficiency ( $\eta_{ED}$ ), charge collection efficiency ( $\eta_{CC}$ ), internal quantum efficiency ( $\eta_{IQE}$ ), absorption efficiency ( $\eta_a$ ), and external quantum efficiency ( $\eta_{EQE}$ ).

## 4.0 RESULTS AND DISCUSSION

### 4.1 Unique Morphology of Hybrid Nanocomposites Deposited by RIR-MAPLE Polymer Thin Films Deposited by RIR-MAPLE: Crystallinity and Orientation

The hole drift mobilities of thin films of poly[2-methoxy-5-(2'-ethyl-hexyloxy)-1,4-phenylene vinylene] (MEH-PPV) deposited by RIR-MAPLE, drop-casting, and spin-casting were determined by the time-of-flight (TOF) photoconductivity method in order to demonstrate the value added by RIR-MAPLE in terms of improving charge transport. Furthermore, the mobility was measured as a function of temperature and applied electric field for analysis in the frameworks of Bässler's Gaussian disorder model (BGDM) and the correlated disorder model (CDM) in order to correlate the measured mobility to internal morphology and better understand the impact of RIR-MAPLE on the internal morphology of MEH-PPV films. The measurement temperatures for the spin-cast film were varied from 25°C to 55°C in increments of 5°C, and the measurement temperatures for the drop-cast and RIR-MAPLE-deposited films were varied from 20°C to 50°C in



increments of 5°C. A sample of the measured TOF photocurrent transients for the three investigated film deposition techniques is shown in **Figure 2**. The time at which a peak occurs in the measured current transient corresponds to the transit time,  $\tau$ , which represents the amount of time required for the dissociated holes to traverse the device from contact to contact. The measured transit times are used to determine the associated hole drift mobilities along with the sample thickness and the applied electric field.

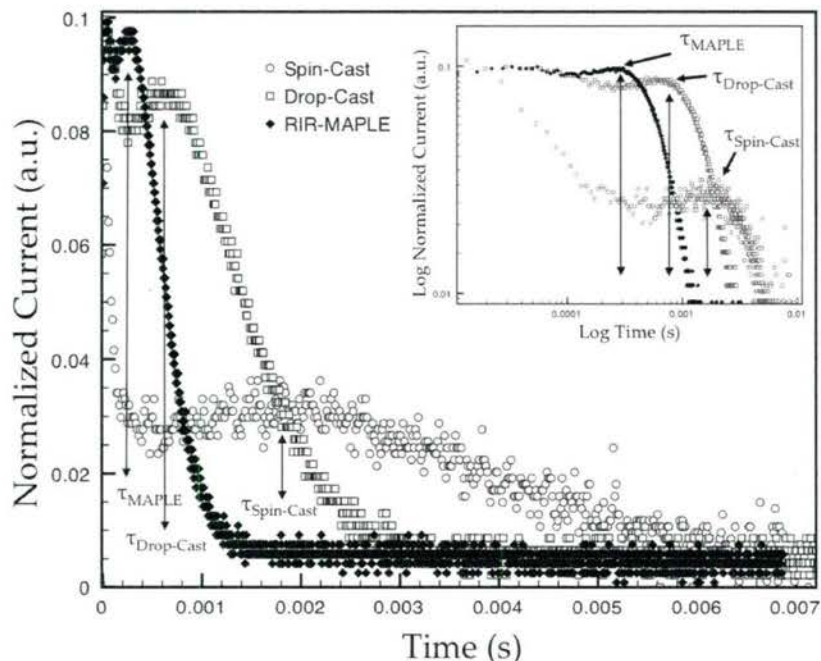


Figure 2. TOF photocurrent transients of spin-cast, drop-cast, and RIR-MAPLE-deposited MEH-PPV films at 30°C and an applied field of 510 (V/cm)<sup>1/2</sup>. The inset shows the same transients on a log-log scale.

The hole drift mobilities for spin-cast, drop-cast, and RIR-MAPLE-deposited MEH-PPV films are shown in **Figure 3** as a function of the square root of the applied electric field for each measurement temperature. It is important to note that the mobility is plotted against  $E^{1/2}$  because it is advantageous for the disorder model analysis used to correlate mobility to internal morphology. For all three deposition techniques, the hole drift mobility increases with increasing applied electric field and with increasing measurement temperature, as expected. The measured hole drift mobilities demonstrate that RIR-MAPLE deposition yields the highest hole drift mobility ( $6.0 \times 10^{-6} \text{ cm}^2/\text{Vs}$  at 25°C and  $2.5 \times 10^5 \text{ V/cm}$ ), whereas drop-cast ( $2.5 \times 10^{-6} \text{ cm}^2/\text{Vs}$  at 25°C and  $2.5 \times 10^5 \text{ V/cm}$ ) and spin-cast depositions ( $1.1 \times 10^{-6} \text{ cm}^2/\text{Vs}$  at 25°C and  $2.5 \times 10^5 \text{ V/cm}$ ) yield lower hole drift mobilities. Importantly, RIR-MAPLE yields higher hole-drift mobility compared to any measured spin-cast film, which is relevant in that spin-casting is often used for the fabrication of conjugated polymer-based photodetectors and photovoltaic solar cells.



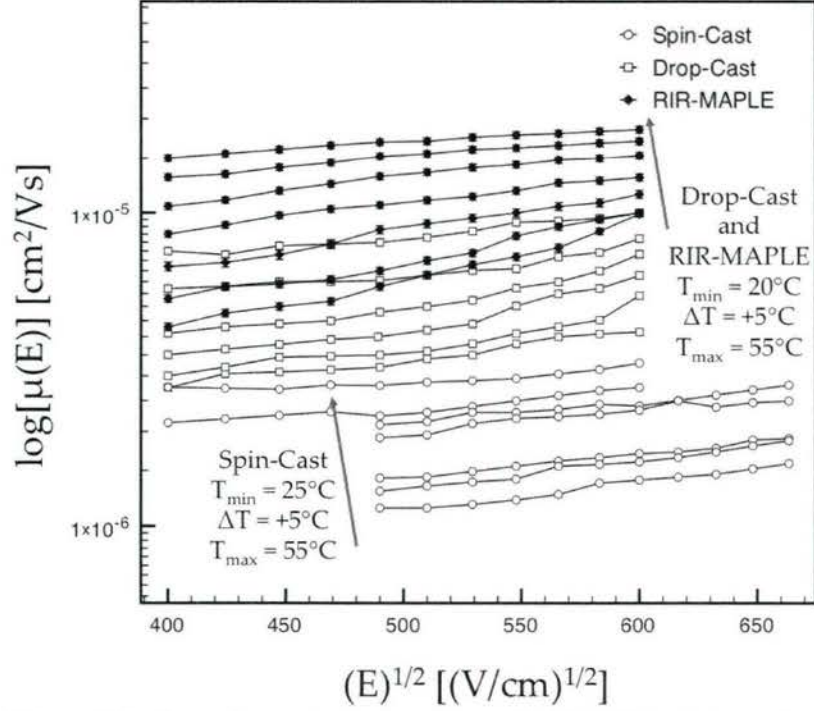


Figure 3. Hole drift mobility for spin-cast, drop-cast, and RIR-MAPLE-deposited MEH-PPV thin films as a function of the square root of the electric field for multiple measurement temperatures.

The measured mobility values are related to the internal morphology of each film by using the BGDM and the CDM. According to the BGDM, the energy distribution of hopping states is Gaussian and the energy levels of adjacent sites are uncorrelated. The primary difference in the CDM is that the energy distribution of hopping states for adjacent molecules is correlated with the spatial positions of chain sites. Each disorder model yields a corresponding energy disorder parameter,  $\sigma$ , which describes the energy required for a charge carrier to hop between adjacent sites in the polymer film. Therefore, smaller values of  $\sigma$  indicate more relaxed polymer chains. The positional disorder parameter,  $\Sigma$ , describes the fluctuation in the distance and orientation of the hopping sites associated with hopping charge carriers. Therefore, decreasing values of  $\Sigma$  indicate increasing film homogeneity on a sub-nanometer scale. The hopping distance between two adjacent sites is  $a$ , and smaller values of  $a$  also indicate more relaxed polymer chains and closer interchain interaction. Thus, in order to extract information about the MEH-PPV film internal morphology from the measured hole drift mobility data, the BGDM is used to calculate the energy disorder parameter,  $\sigma_{BGDM}$ , and the positional disorder parameter,  $\Sigma$ , while the CDM is used to calculate  $\sigma_{CDM}$  and the hopping distance,  $a$ . By determining the disorder parameters using both models, a more complete picture of the polymer film internal morphology is obtained. The BGDM and CDM disorder parameters are summarized in **Table 1**. The overall picture provided by these disorder parameters is that, in comparison to spin-cast and drop-cast MEH-PPV films, RIR-MAPLE-deposited MEH-PPV films exhibit an internal morphology comprising more relaxed and ordered polymer chains with lower hopping energies and lower hopping distances.

Table 1. The disorder model parameters for spin-cast, drop-cast, and RIR-MAPLE-deposited MEH-PPV thin films.

Deposition Technique	BGDM energy disorder ( $\sigma_{BGDM}$ , eV)	CDM energy disorder ( $\sigma_{CDM}$ , eV)	BGDM positional disorder ( $\Sigma$ )	CDM hopping distance ( $a$ , Å)
Spin-Cast	0.114	0.126	3.87	8.9
Drop-Cast	0.096	0.106	3.14	6.8
RIR-MAPLE	0.085	0.094	2.64	4.7

In general, there are two possible orientations for P3HT thin films: one in which the  $\pi$ -stacking direction is perpendicular to the substrate surface, or the out-of-plane (OOP) direction, known as the “face-on” orientation; and one in which the  $\pi$ -stacking direction is parallel to the substrate surface, or the in-plane (IP) direction, known as the “edge-on” orientation. The value of the polymer lattice constant can vary in these two directions due to the chain packing and crystallite orientation within the film. Grazing-incidence, wide-angle X-ray scattering (GIWAXS) measurements used to conduct structural studies of solution-cast P3HT films have demonstrated that, without substrate surface treatment, polymer chain self-organization is dominated by crystalline regions with the “edge-on” orientation. However, as shown in **Figure 4**, this is not the case with RIR-MAPLE films, which are more amorphous and isotropic with comparable “edge-on” and “face-on” orientations.

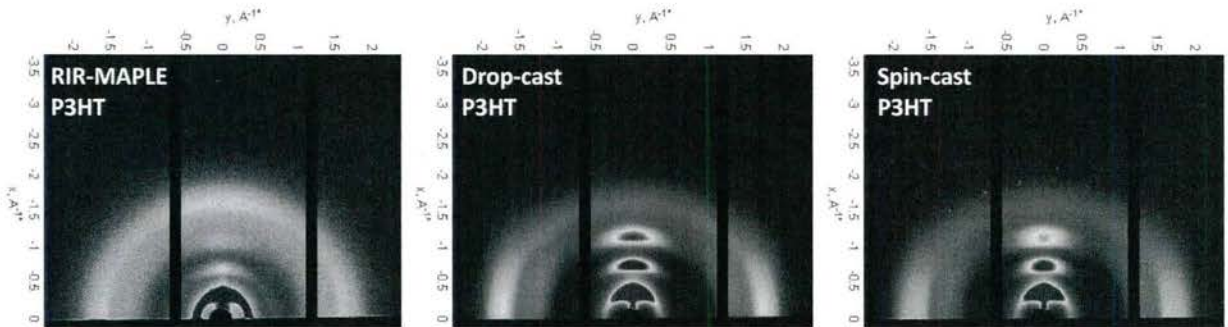


Figure 4. Two-dimensional GIWAXS measurements of a representative RIR-MAPLE-deposited P3HT thin film compared with drop-cast and spin-cast P3HT thin films. RIR-MAPLE parameters are: 7 cm TS distance; with SDS; annealed at 140 C for 30 minutes.

### **Hybrid Nanocomposite Thin Films Deposited by RIR-MAPLE: Percolation Threshold**

Nanocomposite thin films present a greater challenge to using TOF photoconductivity measurements for two important reasons. First, the net absorption coefficient of the film depends on the characteristics of the CQDs incorporated into the nanocomposite. Therefore, the absorption coefficient of the nanocomposite film may decrease to the point where there is insufficient photogenerated charge to measure a transient current. Furthermore, the comparison of nanocomposites with different CQD concentrations is very difficult. Second, hybrid nanocomposites do not yield a thin sheet of photogenerated charge because exciton dissociation occurs throughout the laser pulse absorption volume



due to polymer-CQD interfaces. As a result, the accurate extraction of the transit time from the photocurrent transient is extremely challenging.

In order to resolve these issues, a modified TOF method was developed using a two-layer film: a laser-absorbing layer consisting of pure MEH-PPV and a second layer consisting of the nanocomposite to be measured. The hole transit time of the pure polymer component is subtracted from the hole transit time of the entire two-layer system, yielding the transit time of just the nanocomposite component ( $\tau_{\text{nanocomposite}} = \tau_{\text{heterostructure}} - \tau_{\text{pure polymer}}$ ). This nanocomposite hole transit time can then be used to measure the hole drift mobilities and to extract the internal morphology of the polymer in hybrid nanocomposites by using the BGDM and the CDM. **Figure 5** summarizes the modified TOF method that was developed in this work.

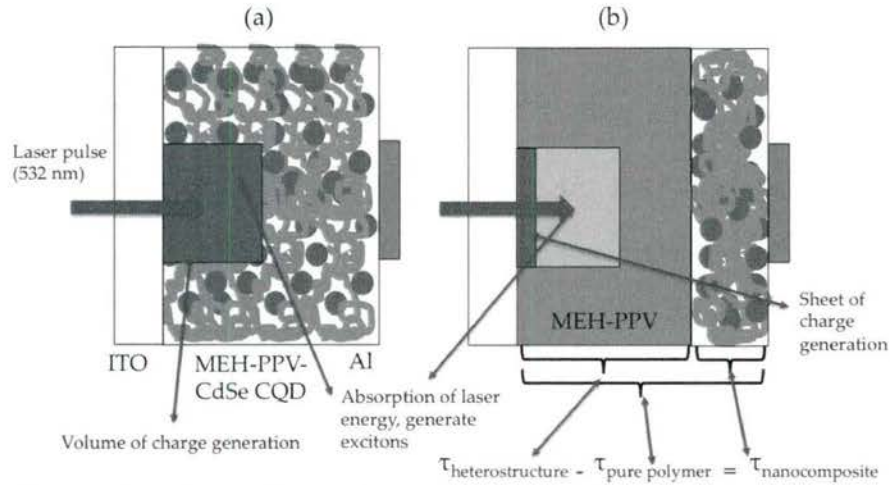


**Figure 5.** (a) Due to deep laser absorption and excitonic dissociation in the nanocomposite, a volume of charge is photogenerated and the TOF transit time cannot be accurately extracted from the resultant current transient. (b) The modified TOF method uses a layered structure that consists of a pure MEH-PPV laser absorbing layer and a MEH-PPV-CdSe CQD transport layer.

The transit time of the pure MEH-PPV layer is subtracted from the transit time of the entire heterostructure to find the transit time of the nanocomposite layer.

Two-layer films comprising MEH-PPV and MEH-PPV:CdSe CQD hybrid nanocomposites were deposited on ITO-coated glass substrates. The nanocomposites were deposited using RIR-MAPLE with different CQD concentrations. The wt% ratios for MEH-PPV:CdSe CQDs were 100:0, 80:20, 60:40, 40:60, and 20:80 and the final film thickness (including the drop-cast MEH-PPV film) was  $6.5 \pm 0.10 \mu\text{m}$ . The nanocomposite layer thickness for each dot concentration ratio was approximately  $1.0 \pm 0.05 \mu\text{m}$ . Each heterostructure was characterized by temperature- and electric field-dependent TOF measurements. The results of the temperature- and electric field-dependent hole drift mobility measurements are summarized in

**Figure 6**, where the general trend is that as the CdSe CQD content in the hybrid nanocomposite films increases, the hole drift mobility of the polymer decreases. Furthermore, as expected, all measured drift mobilities increase with increasing temperature and electric field.

The BGDM and CDM energy disorder parameters ( $\sigma$ ), BGDM positional disorder parameters ( $\Delta$ ), and CDM hopping distances ( $a$ ) for the different MEH-PPV:CdSe CQD



ratios are summarized in **Table 2**. These parameters explain the origin of decreasing hole drift mobility in MEH-PPV as a function of increased CdSe CQD concentration in the hybrid nanocomposites. As more CQDs are added to the polymer bulk, the polymer chains are pushed farther away from one another such that the average hopping distance increases and the corresponding energy per hop increases (on the order of 13.1 Å and 0.170 eV, respectively, for the 20:80 MEH-PPV:CdSe CQD case).

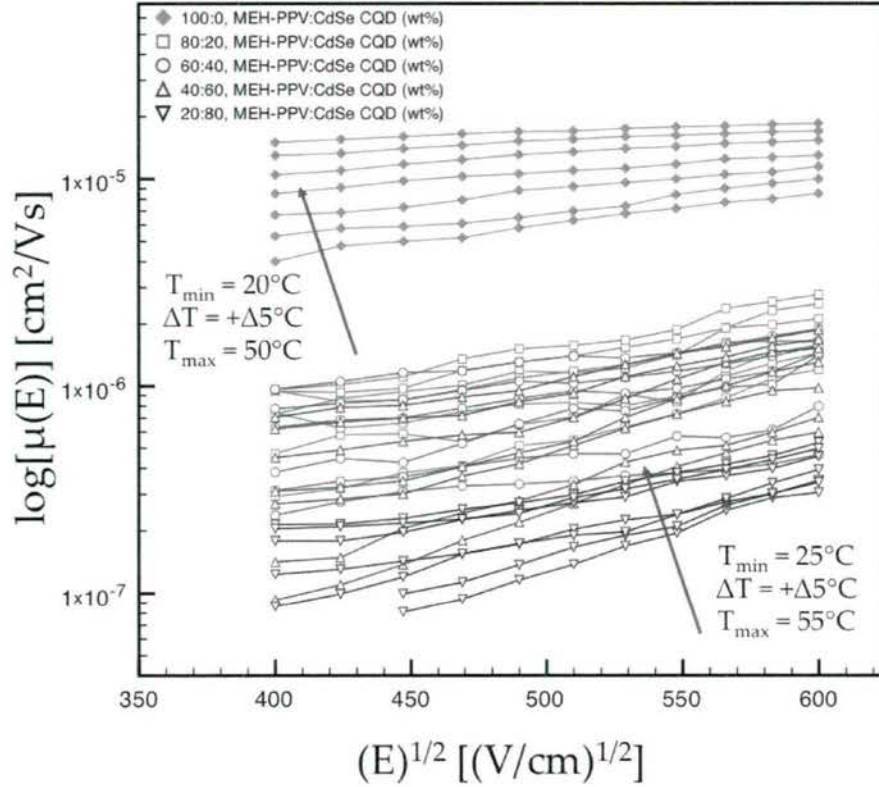


Figure 6. Hole drift mobility vs. temperature and electric field for nanocomposite thin films with different MEH-PPV:CdSe CQD ratios.

Table 2. The BGDM and CDM energy disorder parameters, BGDM positional disorder parameters, and CDM hopping distances of MEH-PPV-CdSe CQD thin films with different MEH-PPV:CdSe ratios.

MEH-PPV:CdSe ratio (%)	BGDM energy disorder para. ( $\sigma$ , eV)	CDM energy disorder para. ( $\sigma$ , eV)	BGDM positional disorder parameter ( $\Sigma$ )	CDM hop distance ( $a$ , Å)
100:0	0.085	0.094	2.64	4.7
80:20	0.106	0.118	3.74	6.3
60:40	0.126	0.140	3.46	8.2
40:60	0.134	0.149	4.44	9.5
20:80	0.153	0.170	4.91	13.1

This study has very important implications for the application of polymer-CQD bulk heterojunctions to photovoltaic solar cells. The electron percolation threshold for hopping conduction in solution-cast nanocomposites is approximately 50 vol% to 65 vol% of the electron transporting material (in this case, the CdSe CQD) relative to the polymer bulk; hence, in the context of this study, a 50:50 MEH-PPV:CdSe vol% ratio is approximately 15:85 MEH-PPV:CdSe wt% (MEH-PPV, density of 0.98 g/cm and CdSe, density of 5.82 g/cm), which is still slightly more CdSe-rich than the maximum MEH-PPV:CdSe ratio (20:80) investigated in this TOF measurement. As solar cell results will show, hybrid nanocomposite thin films deposited by RIR-MAPLE can reach this percolation threshold for a lower weight percent of CQDs due to the fundamentally different film morphology. The long term implications for such a result are that RIR-MAPLE is a more efficient process and less wasteful in the use of CQDs.

#### **Hybrid Nanocomposite Thin Films Deposited by RIR-MAPLE: Solvent Independence and Dispersion with Short-Chain Ligands**

The typical nanoparticle material system used in hybrid nanocomposites for this work was CdSe CQDs with trioctylphosphine oxide (TOPO) long-chain ligands that are exchanged for pyridine (PY) short-chain ligands. To observe, directly, the nanoparticle component of the PCPDTBT/CdSe hybrid nanocomposite films, transmission electron microscopy (TEM) was used to investigate the impacts of different ligands (TOPO vs pyridine), different solvents (chlorobenzene vs dichlorobenzene vs trichlorobenzene), and different deposition methods (RIR-MAPLE vs spin-casting) on the morphology of the blended films. First, TEM images of the PCPDTBT/TOPO-capped CdSe nanocomposite film (80 wt% CdSe loading) deposited by spin-casting and RIR-MAPLE were studied. The hybrid nanocomposite films spin cast from chlorobenzene, dichlorobenzene, and trichlorobenzene (using two different size scales) are shown in **Figure 7(a, d)**, **Figure 7(b, e)** and **Figure 7(c, f)** respectively. Clearly, the blended films spin-cast from all three solvents show nanoparticle segregation with a certain pattern. For the hybrid nanocomposite film spin cast from chlorobenzene (**Figure 7(a, d)**), a number of circular clusters (diameters of 100 nm to 200 nm) with high nanoparticle concentration are observed to be scattered across the film, and the PCPDTBT has no particular structure. When the hybrid nanocomposite film is spin cast from dichlorobenzene (**Figure 7(b, e)**), the clusters of nanoparticles are less circular and have lower concentrations of nanoparticles. In addition, the PCPDTBT becomes more structured, as evidenced by the emergence of fiber-like features in the film. When trichlorobenzene is used as the solvent, the clusters of nanoparticles are no longer prominent, and the fiber-like structure of the polymer is well-defined (**Figure 7(c, f)**). The observed phase segregation in spin cast films is due to the different polarity of the polymer and nanoparticles, as well as their interaction within a specific solvent. For example, the boiling point of the solvent affects the phase segregation that occurs while the film is drying. Trichlorobenzene has the highest boiling point (213 °C) in this study; thus, the solvent evaporation rate is the slowest for hybrid nanocomposites spin cast from this solvent. The slow drying of the film allows the PCPDTBT polymer chains to rearrange themselves and form a thermodynamically stable morphology, which is the fiber-like structure observed. Clearly, the phase segregation of



CdSe nanoparticles and PCPDTBT is strongly dependent on the chosen solvent in spin cast films.

To compare with spin cast films, TEM images of PCPDTBT/TOPO-capped CdSe hybrid nanocomposite films (80 wt% CdSe target ratio) deposited from RIR-MAPLE using chlorobenzene, dichlorobenzene, and trichlorobenzene as primary solvents (using the same two size scales) are shown in **Figure 7(g, j)**, **Figure 7(h, k)** and **Figure 7(i, l)** respectively. In contrast to the spin cast blended films, the hybrid nanocomposite films deposited by RIR-MAPLE do not yield significantly different nanoparticle distributions within the polymer for different primary solvents. In addition, no clear patterns of nanoparticle and polymer rich domains are observed. The distribution of nanoparticles can be described as random and uniform, and it is independent of the chosen primary solvent.

In hybrid nanocomposite solar cells, the pyridine-capped CdSe nanoparticles are used as electron acceptors due to better charge transport properties compared to TOPO-capped CdSe nanoparticles. For this reason, TEM images of the PCPDTBT/pyridine-capped CdSe hybrid nanocomposite films deposited by spin-casting and RIR-MAPLE are shown in **Figure 8**. For both deposition methods, trichlorobenzene is used as the solvent or primary solvent. As can be seen, no significant difference between the two deposition techniques is observed from the TEM images of both films on the smallest scale (**Figure 8(a, d)**). However, when the size scale is larger, the nanoparticle aggregation shows up as black clusters in the spin cast film (**Figure 8b**), whereas the RIR-MAPLE deposited film does not change significantly, though some much smaller clusters can be observed (**Figure 8e**). The aggregation of CdSe nanoparticles in the spin cast film becomes even more obvious when examining the TEM images in the micron scale (**Figure 8c**), while the RIR-MAPLE deposited film does not change significantly on this large scale (**Figure 8f**). Clearly, the RIR-MAPLE deposition leads to a blended film with less aggregation of CdSe nanoparticles. It is interesting to note that the fiber-like structures of PCPDTBT do not appear in the spin cast PCPDTBT/pyridine-capped CdSe hybrid nanocomposite film, which may due to the low contrast of the fiber-like structure from the background in the presence of aggregation of the pyridine-capped CdSe (large black features in the image). Thus, RIR-MAPLE shows the capability to improve the dispersion of nanoparticles by minimizing the solvent evaporation process.

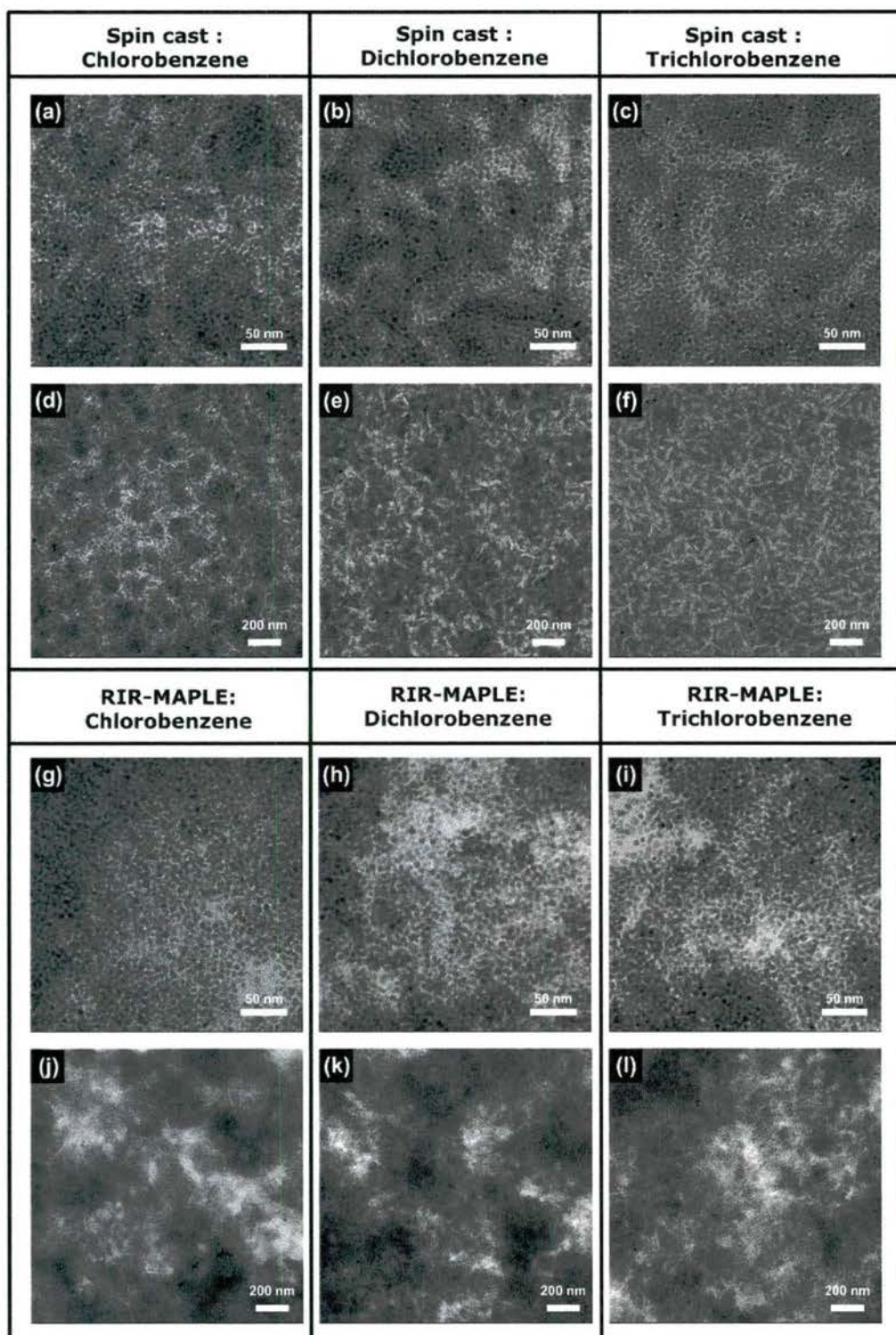


Figure 7. TEM images of PCPDTBT/TOPO-capped CdSe hybrid nanocomposite films deposited by spin-casting using (a)(d) chlorobenzene, (b)(e) dichlorobenzene, (c)(f) trichlorobenzene as the solvent and deposited by RIR-MAPLE using (g)(j) chlorobenzene, (h)(k) dichlorobenzene, (i)(l) trichlorobenzene as the primary solvent. The scale bars are labeled on the images.



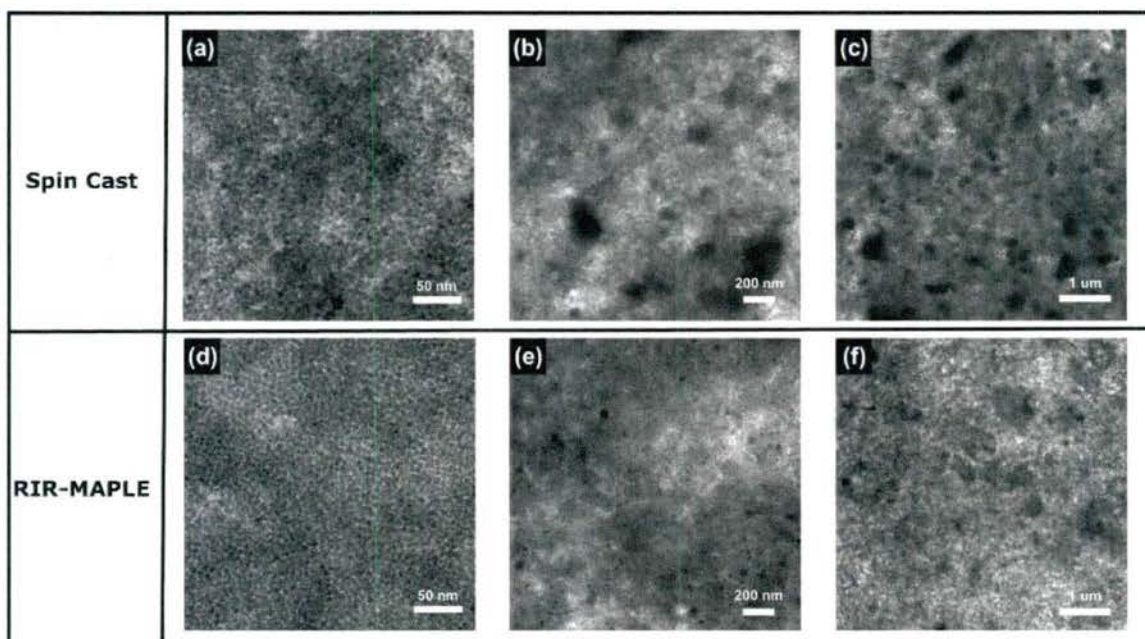


Figure 8. TEM images of PCPDTBT/pyridine-capped CdSe hybrid nanocomposite films deposited by (a) (b)(c) spin-casting using trichlorobenzene as the solvent and deposited by (d)(e)(f) RIR-MAPLE using trichlorobenzene as the primary solvent. The scale bars are labeled in the images.

## 4.2 Multi-spectral, Hybrid Nanocomposite Infrared Photodetectors Deposited by RIR-MAPLE

### Intraband Absorption Coefficients in Hybrid Nanocomposites

A model was developed to calculate quantized energy levels in semiconductor nanoparticles, as well as oscillator strengths such that the most likely intraband transitions can be compared to measured Fourier transform infrared (FTIR) intraband absorption spectra. Importantly, this model includes the influence of organic surface ligands such that the impact of surface ligand exchange and removal can be compared to experimental results. In the model, the radial potential profile for the nanocomposite, including organic surface ligands, is represented by the schematic diagram shown in **Figure 9**. The Schrödinger equation is solved for this potential using spherical coordinates and the transfer matrix method. The transition rate from any initial to final energy state due to the absorption of a photon is determined using the Fermi golden rule. Finally, the contribution to the absorption coefficient from all possible energy transitions for a CQD with radius  $r_0$  is determined assuming a Gaussian size distribution in the total CQD ensemble.

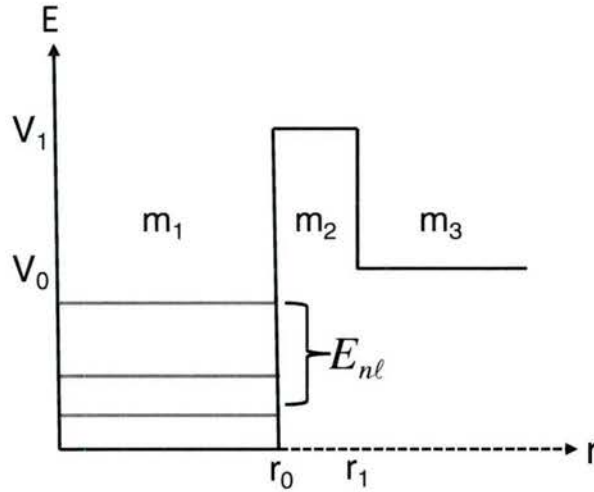


Figure 9. Schematic representation of finite spherical potential for CdSe/surface ligand/MEH-CN-PPV nanocomposite.

In order to determine the efficacy of this model, the calculated absorption coefficient is compared with the measured FTIR absorbance spectrum for a CdSe/ODA/MEH-CN-PPV nanocomposite thin film on a p-type GaAs substrate. The ligand length for ODA is determined by the C-C (1.54 Å) and C-N (1.47 Å) bond lengths, the effective mass for the CQD is that of bulk CdSe, the potential offset for MEH-CN-PPV is taken from literature, the assumed values for the mean CQD radius and size distribution are provided by the manufacturer, NN Labs Inc., and the effective mass for MEH-CN-PPV is assumed to be that of the free electron. The mean CQD radius was allowed to vary over a small range around the published value and the unknown variables (ligand potential offset and effective mass) were used to fit the calculated absorption coefficient to the measured intraband peaks. The comparison of the calculated and measured data is shown in **Figure 10** along with the fitting parameters. The measured absorbance peaks at ~0.22 and ~0.43 eV were determined to be due to intraband absorption in the conduction band of the CdSe CQDs. From this figure it can be seen that the relative peak heights fit very well and the peak energies correspond well with a percent error for peak 1 of 2.27% and for peak 2 of 0.11%.

The effect of various ligands on the calculated absorption coefficient, assuming the same material parameters for the CdSe CQD and MEH-CN-PPV polymer, is of interest as a method for optimizing device performance. When comparing ligand materials, the pertinent parameters are the ligand length ( $r_1 - r_0$ ), ligand potential offset ( $V_1$ ), and ligand effective mass ( $m_2$ ). The ligand length is determined by the bond lengths for C-C (1.54 Å), C-N (1.47 Å), C=C (1.34 Å), and C-O (1.43 Å); however, the lack of values for the potential offset and effective mass in the literature leads to the assumption that these values are the same as those from the fit shown in **Figure 10**. This assumption is reasonable because the ligand structures are similar and, thus, the material parameters should not change appreciably from ligand to ligand. The ligand materials and parameters we have compared are shown in **Table 3** and the normalized absorption coefficient for each ligand material is shown in **Figure 11**.



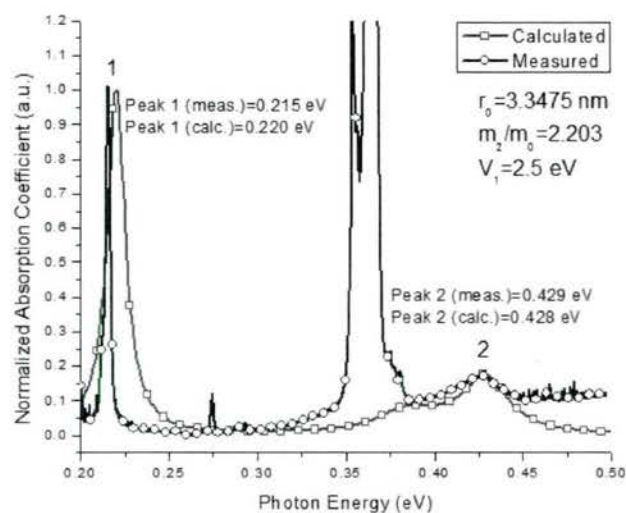


Figure 10. Comparison of normalized calculated absorption coefficient and measured absorbance.

Table 3. Model parameters for surface ligand materials.

Surface Ligand Material	Ligand Length (nm)	V1 (eV)	m2/m0
Pyridine	0.308	2.5	2.203
Butylamine	0.497	2.5	2.203
Octylamine	1.000	2.5	2.203
Dodecylamine	1.378	2.5	2.203
Oleic Acid	2.000	2.5	2.203
Octadecylamine	2.258	2.5	2.203

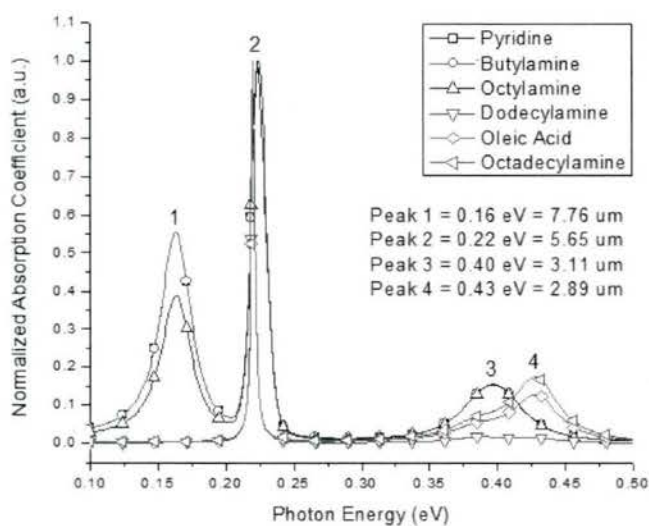


Figure 11. Comparison of normalized absorption coefficient for various ligand materials.

From **Figure 11** it can be seen that, for the shortest ligand materials, peak 4 is suppressed and peaks 1 and 3 are enhanced. As the ligand length increases, peak 1 disappears and peak 4 becomes stronger, whereas for all ligand materials the strongest peak occurs at  $\sim 0.23$  eV. The normalized absorption coefficient can be utilized to determine where a device would be sensitive in the IR, however, it is also important to consider how the absorption strength changes with an increase in the ligand length. **Figure 12** shows how the absorption coefficient values change for each surface ligand material. From this figure it can be seen that the absorption strength of the nanocomposite material is extremely sensitive to the length of the surface ligand material. This can have a profound effect on the responsivity of a device and it is clear that utilizing the shortest ligand material possible is optimal for improving device performance.

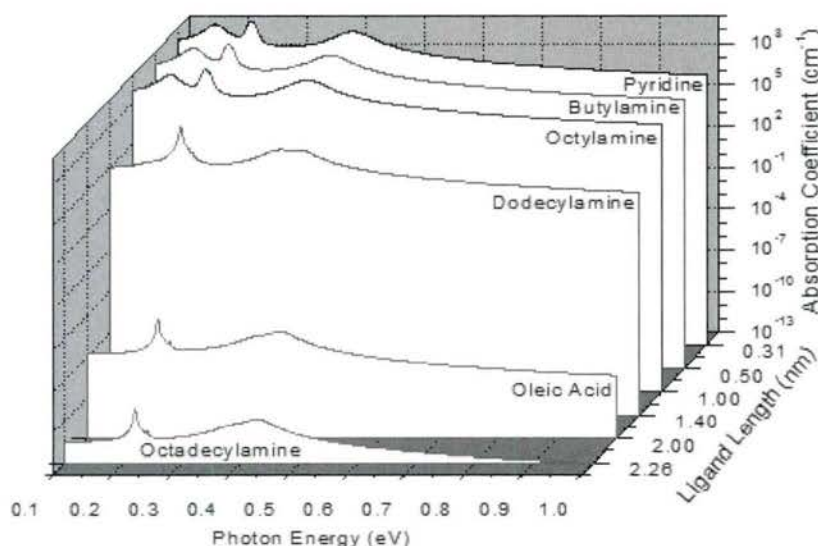


Figure 12. Comparison of absorption coefficient for various ligand materials.

### **Multi-spectral Hybrid Nanocomposite Infrared Photodetectors Enabled by RIR-MAPLE Deposition of *In-situ* Polymerized Nanocomposites**

For this work, dispersed nanocomposites were prepared by the photopolymerization of 2-aminoethyl methacrylate hydrochloride (AEM) precursor in a blend of trioctyl phosphine oxide (TOPO)-capped CdSe CQDs and poly(2-methoxy-5-(2'-ethylhexyloxy)- $\alpha,\alpha'$ -dicyano-*p*-xylylidene-alt-2,5-dihexyloxy-*p*-xylylidene) (MEH-CN-PPV). AEM was photopolymerized by exposing an AEM solution to two hours of UV irradiation, and successful photopolymerization was verified using  $^1\text{H}$  NMR spectroscopy and FTIR absorption spectroscopy. In order to demonstrate the improved dispersion of the hybrid nanocomposite prepared by *in-situ* polymerization, four samples were prepared in chloroform as shown in **Figure 13**: (Sample 1) a CdSe CQD and MEH-CN-PPV blend at a weight ratio of 5:1, respectively (typical nanocomposite preparation); (Sample 2) a CdSe CQD, MEH-CN-PPV, and AEM monomer blend at a weight ratio of 5:1:1, respectively; (Sample 3) a CdSe CQD, MEH-CN-PPV, and polyAEM (PAEM) blend at a weight ratio of 5:1:1, respectively; and (Sample 4) an *in-situ* photopolymerized CdSe CQD, MEH-CN-PPV, and AEM monomer blend at a weight ratio 5:1:1, respectively. The observed



aggregation and dispersion of the CQDs and polymer units for each of the samples are also depicted in **Figure 13**. Samples 1 and 4, i.e. typical hybrid nanocomposite and the *in-situ* polymerized nanocomposite, are discussed in more detail in the following.

TEM images for Samples 1 and 4 are shown in **Figure 14** as they represent extremes of the observed morphologies. Sample 1 (**Figure 14a**) exhibited poor dispersion with agglomeration of CdSe CQDs in the MEH-CN-PPV polymer matrix. Sample 4 (**Figure 14b**) exhibited sphere-like structures with dispersed single CQDs within the sphere, as shown in the magnified image in **Figure 14c**. Well-dispersed CQDs are scattered in each sphere. Though the spheres were random in size, the average size of the spheres was about 400 nm. The sphere-shaped nanocomposite of Sample 4 was stained with OsO<sub>4</sub> in order to distinguish the location of MEH-CN-PPV and PAEM in the spherical matrix. The OsO<sub>4</sub> stained sphere image is shown in **Figure 14d**. The MEH-CN-PPV domain is darker due to the OsO<sub>4</sub> staining (osmium blocks electron beam) and the PAEM domain appears white in the image. This image shows that the photopolymerized AEM wraps around the spheres of the CdSe CQDs/MEH-CN-PPV nanocomposite.

As a second demonstration of improved dispersion of CQDs resulting from *in-situ* polymerization, Förster resonance energy transfer (FRET) was characterized using time-resolved photoluminescence (TRPL) measurements of the donor (MEH-CN-PPV) because the temporal photoluminescence decays faster in those films with better dispersion of the acceptor (CdSe CQDs) due to increased FRET. FRET is modified by controlling the overlap of the donor (conjugated polymer) emission spectrum and acceptor (CQD) absorption spectrum, as well as the distance between the donor and the acceptor components. Therefore, higher FRET implies that dot aggregation is not present (because the resulting spectral shifts would yield a smaller overlap integral) and that the physical distance between donors and acceptors is reduced. The TRPL spectra for the four nanocomposite samples and a reference MEH-CN-PPV sample are shown in **Figure 15**, and the corresponding TRPL decay lifetimes are shown in the inset. All of the nanocomposite samples exhibited shorter decay lifetimes ( $\tau_1$ ) than the reference MEH-CN-PPV film (pink line,  $\tau_1 = 0.89$  ns) due to FRET from the MEH-CN-PPV to the CdSe CQDs. In comparing the standard hybrid nanocomposite (Sample 1) to the hybrid nanocomposite prepared using *in-situ* polymerization (Sample 4), the decay lifetime of Sample 1 (black line,  $\tau_1 = 0.67$  ns) is much greater than that of Sample 4 (green line,  $\tau_1 = 0.46$  ns), indicating enhanced dispersion resulting from the *in-situ* polymerization.

These nano-spherical encapsulated nanocomposites should be studied further by controlling the blend ratio and the CQD numbers in the sphere to arrange CQDs and increase the number of CQDs in the sphere. Such spherical nanocomposites could enable a broad selection of CQD and polymer constituent materials, which is beneficial for tuning nanocomposite optoelectronic properties. Also, well-dispersed CQDs in sphere-shaped nanocomposite increases charge transfer efficiency so that enhanced performance of photodetectors and photovoltaic solar cells could be achieved by *in-situ* polymerization using a third monomer source.

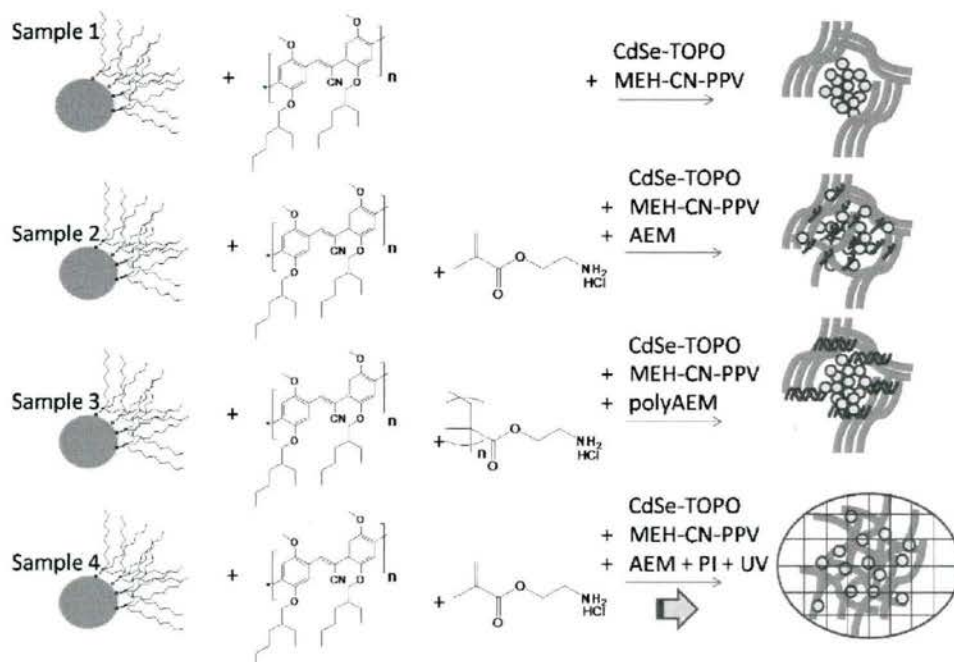


Figure 13. The preparation and observed morphology of four different hybrid nanocomposite samples designed to investigate CQD dispersion.

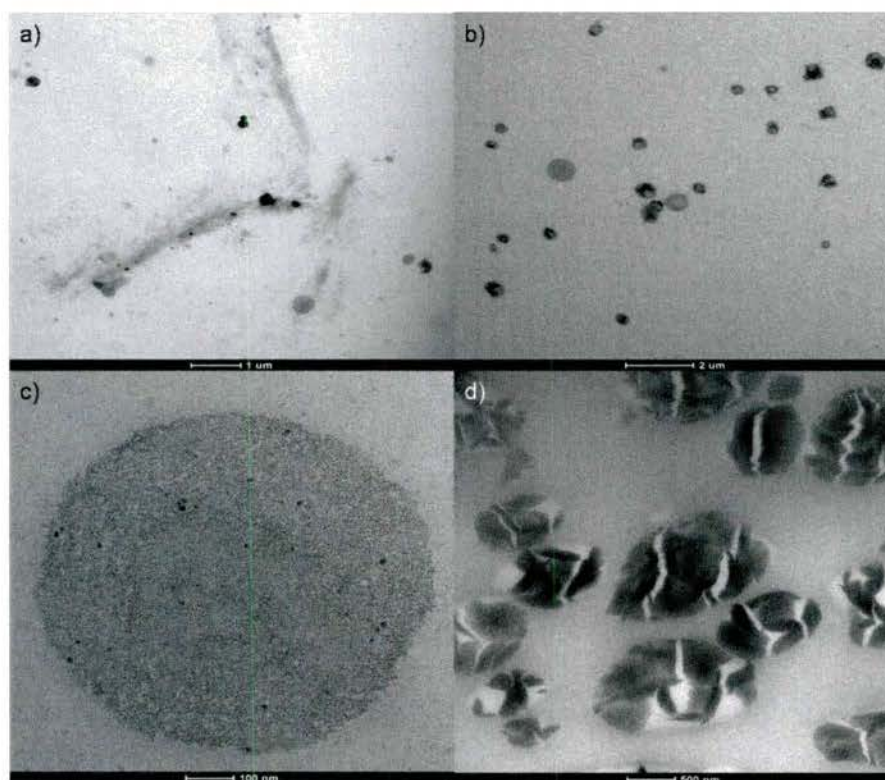


Figure 14. TEM images of nanocomposites: (a) Sample 1 and (b) Sample 4; (c) magnified image of Sample 4 demonstrating dispersed CdSe CQDs within the polymer matrix; and (d) OsO<sub>4</sub>-stained Sample 4 demonstrating location of MEH-CN-PPV and PAEM.



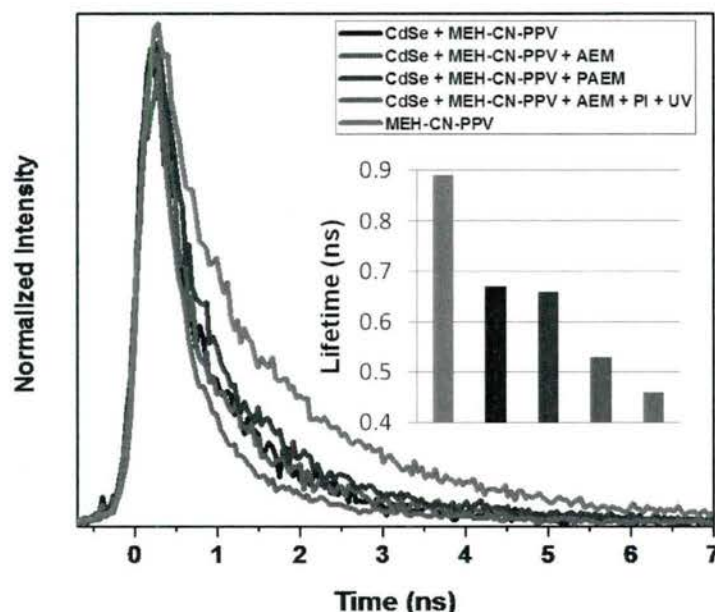


Figure 15. TRPL spectra (excited at 405 nm, 1.5  $\mu$ W, measured in 530-555 nm) of the four nanocomposite samples in solid state and a reference MEH-CN-PPV film. The measured TRPL decay lifetimes are shown in the inset.

A multi-spectral, hybrid nanocomposite photodetector [visible and infrared (IR)] was demonstrated at room temperature and provides high responsivity at low bias. The photodetector active regions comprised the *in-situ* polymerized CdSe CQD/MEH-CN-PPV hybrid nanocomposite using free AEM monomer precursors. The device structures were deposited by RIR-MAPLE. An important characteristic of the *in-situ* polymerized hybrid nanocomposites is that the CQD concentration in the sphere-like nanocomposites can be controlled by changing the amount of AEM in the blended solution before photopolymerization. While 10% AEM-precursor yields only sphere-like nanocomposites, 4% AEM-precursor yields the same sphere-like nanocomposites, as well as scattered CQDs interspersed among the sphere-like nanocomposites. The morphologies of typical CdSe CQD/MEH-C-PPV blends and the *in-situ* polymerized nanocomposites deposited by drop-casting and RIR-MAPLE are shown in **Figure 16**. The CdSe/MEH-CN-PPV blend exhibits aggregated CdSe CQDs in both the drop cast and RIR-MAPLE films. In contrast, the CdSe CQDs in the *in-situ* polymerized CdSe CQDs/MEH-CN-PPV nanocomposites featured the sphere-like nanocomposites. Importantly, CdSe CQDs in the 4% AEM-precursor nanocomposite were found in the sphere-like nanocomposite and interspersed outside of the sphere-shapes.

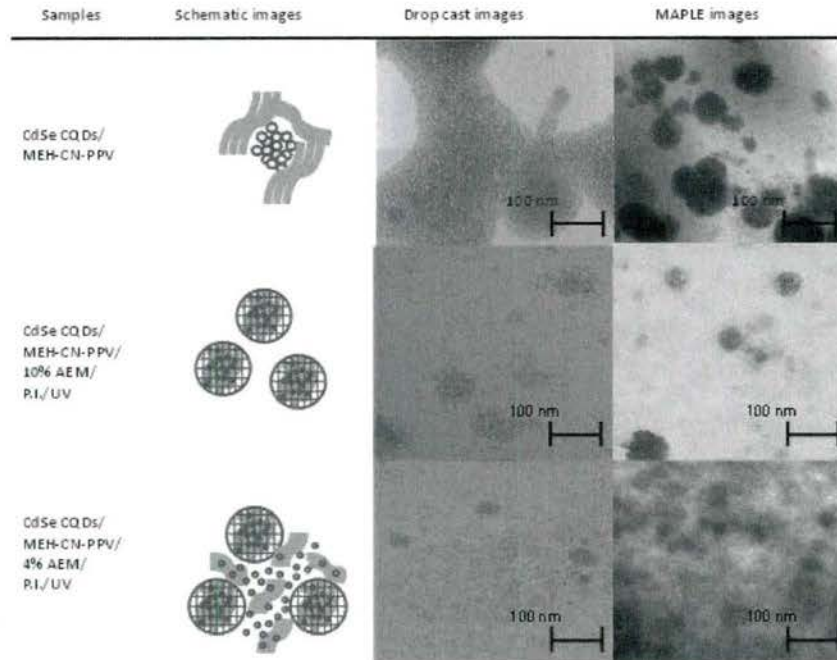


Figure 16. Schematic and TEM images of CdSe CQDs/MEH-CN-PPV blend and in-situ polymerized CdSe CQDs/MEH-CN-PPV nanocomposites.

Using RIR-MAPLE deposition onto transparent ITO glass substrates, vertical geometry photodetectors were fabricated with *in-situ* polymerized hybrid nanocomposite active regions featuring the two different AEM concentrations (10% and 4% AEM-precursor). The active region thickness was approximately 100 nm. Al contacts were evaporated on the nanocomposites. The device with the 4% AEM-precursor nanocomposite active region provided the strongest current signal, so it was characterized using spectral photocurrent measurements. A Xe lamp source was used for the visible spectrum, and a calibrated blackbody was used for the IR spectrum. The excitation wavelength was selected using a monochromator. At each wavelength [visible - 300 nm to 700 nm in 10 nm intervals; IR - 2500 nm to 5500 nm in 20 nm intervals], the average current was determined. A calibrated Si detector was used to estimate the spectral responsivity of the hybrid nanocomposite devices at given applied bias in the range from -2.0 to +2.0 V.

**Figure 17** shows the measured spectral responsivity in the (a) visible and (b),(c) IR regions for the 4% AEM-precursor, *in-situ* polymerized CdSe/MEH-CN-PPV hybrid nanocomposite photodetector. In the visible region, the spectral responsivity peaks at 470 nm and 570 nm are attributed to the absorption of MEH-CN-PPV and CdSe CQDs, respectively, as confirmed by the measured UV-Vis absorption spectrum for the nanocomposite [also shown in **Figure 17a**]. In the IR region, the spectral responsivity peaks at 2850 nm, 3200 nm, and 5100 nm are attributed to electronic intraband transitions in the conduction band of the nanocomposite. FTIR absorbance measurements of the nanocomposites [also shown in **Figure 17(b, c)**] seem to confirm this explanation because the same peaks are observed and there are no vibration sources at 3200 nm and 5100 nm from the organic materials in the nanocomposite. It is important to note that these mid-IR photodetectors operate at room temperature.



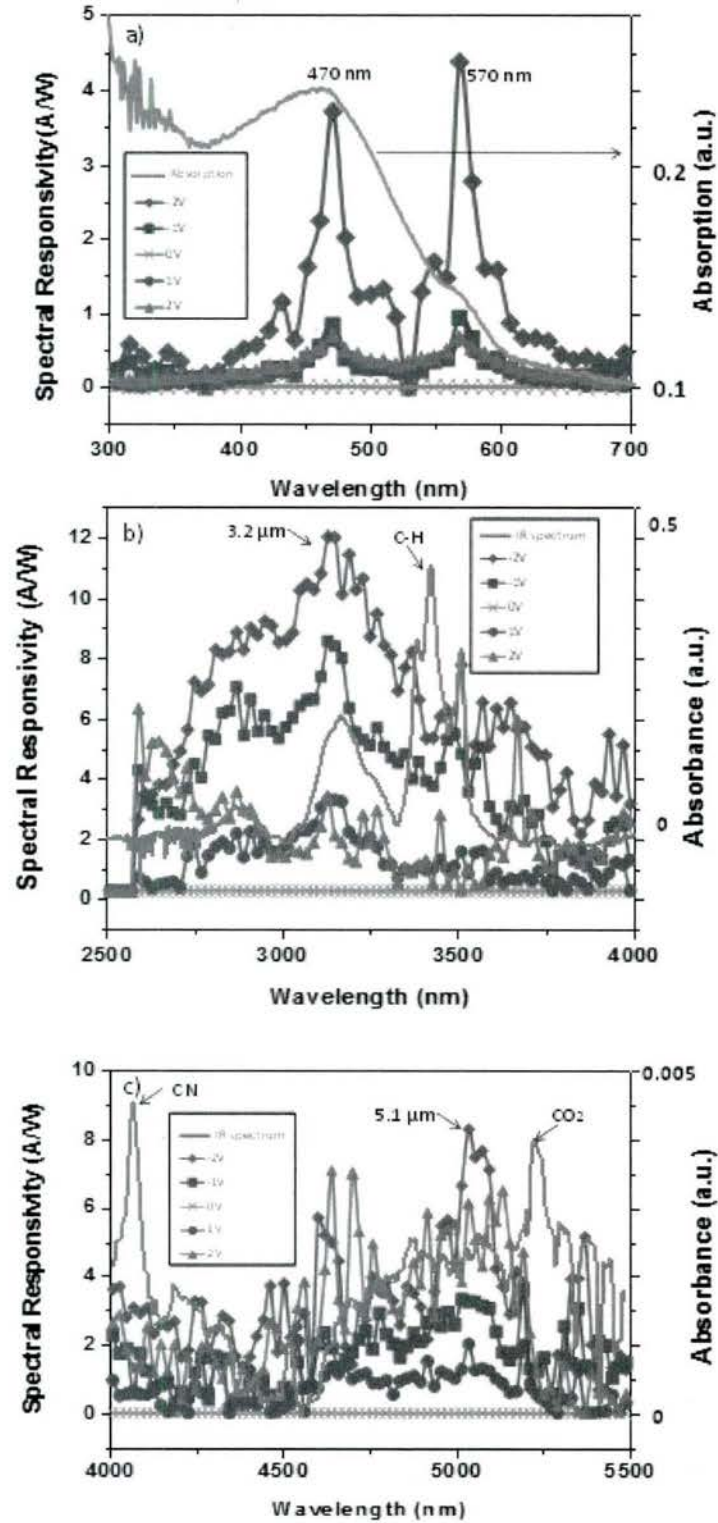


Figure 17. Spectral responsivities of in-situ polymerized CdSe/MEH-CN-PPV hybrid nanocomposite photodetector (4% AEM) in the a) visible region (300 nm to 700 nm); (b) the IR region (2.5  $\mu\text{m}$  to 4  $\mu\text{m}$ ); and c) the IR region (4  $\mu\text{m}$  to 5.5  $\mu\text{m}$ ). The UV-Vis absorption spectrum for the same nanocomposite material is also shown.

### 4.3 Organic and Hybrid Nanocomposite Solar Cells Deposited by RIR-MAPLE

#### Impact of Surfactant and Simultaneous vs. Sequential Deposition Modes on Organic Solar Cells

The maximum amount of surfactant that can be included in the RIR-MAPLE target and still yield photovoltaic function was determined. Ideally, the deposited BHJ solar cells contain two components, the conjugated polymer and the organic small molecule; however, the surfactant (0.001wt% SDS in DI water), which is necessary to stabilize the emulsion in RIR-MAPLE deposition, could be deposited onto the substrate, as well. As a result, the properties of the surfactant, such as being an insulating molecule, could deteriorate the performance of the OSCs, yet further reduction in the amount of surfactant is not practical because the emulsion could experience flocculation. In this study, PCPDTBT:PC71BM (1:1) BHJ OSCs were fabricated using a series of SDS concentrations higher than 0.001wt% (0.01wt%, 0.1wt%, and 1.0wt%) to study the effect of the amount of surfactant on the performance of the solar cells. The purpose of this study was to explore the trade-off between achieving better emulsion quality (with higher concentration of SDS) and degrading OSC performance (due to incorporation of insulating surfactant into the OSC active region by RIR-MAPLE deposition). Sequential deposition recipes were used for PCPDTBT and PC<sub>71</sub>BM. Solar cell J-V curves were taken in air at room temperature with a Keithley 4200 semiconductor characterization system. Illumination was performed using a 1-sun, AM 1.5G spectrum, solar simulator. The J-V curves for the fabricated organic solar cells (OSCs) are shown in **Figure 18**. As can be seen clearly, the increasing concentration of the SDS surfactant degrades the device performance because the films become less conductive (significant reduction of current density is observed). Among the different SDS concentrations, only the 0.001wt% SDS in DI water yields appropriate performance of OSCs, indicating this surfactant concentration is not completely detrimental to the device performance.

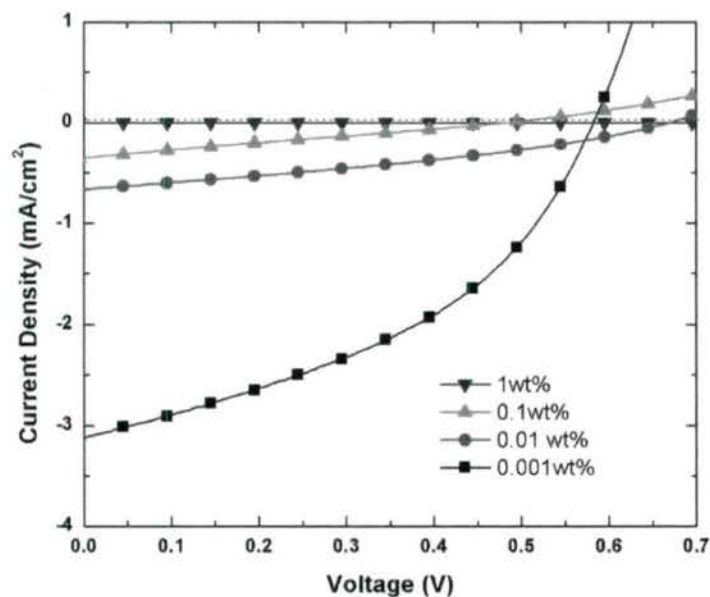


Figure 18. J-V curves of PCPDTBT:PC71BM BHJ OSCs (1:1) deposited by RIR-MAPLE using different SDS weight concentration prepared in DI water.



To investigate the effect of the deposition modes on the performance of OSCs, PCPDTBT/PC<sub>71</sub>BM solar cells with 1:1 ratio were deposited by simultaneous deposition and sequential deposition. Simultaneous deposition uses a single target emulsion containing all the components of the BHJ. The emulsion is injected into the entire target cup and frozen for laser ablation. In contrast, the second deposition mode, known as sequential deposition, uses a separate emulsion for each component. Before freezing the emulsions, the target cup is partitioned into different compartments. To test the performance of BHJ OSCs fabricated by emulsion-based RIR-MAPLE using simultaneous or sequential deposition modes, current density-voltage (J-V) measurements were conducted in each case. Typical J-V curves for the BHJ OSCs deposited by the two deposition modes are shown in **Figure 19a**, and the device performance parameters are listed in the table inset. As can be seen, the BHJ OSCs fabricated by simultaneous deposition showed much lower efficiency (PCE = 0.067%) than the BHJ OSCs fabricated by sequential deposition (PCE = 0.74%). In order to exclude the possibility that the different efficiencies resulted from significantly different BHJ ratios in sequential and simultaneous modes, the UV-Vis-NIR absorbance spectrum of each BHJ active region was measured (**Figure 19b**). The PCPDTBT and PC<sub>71</sub>BM peak intensities in each spectrum were similar, demonstrating comparable absorption from both components. As a result, the large difference in power conversion efficiency for the two deposition modes was not due to different PCPDTBT and PC<sub>71</sub>BM BHJ ratios, but rather how the donor and acceptor molecules were blended together in the film.

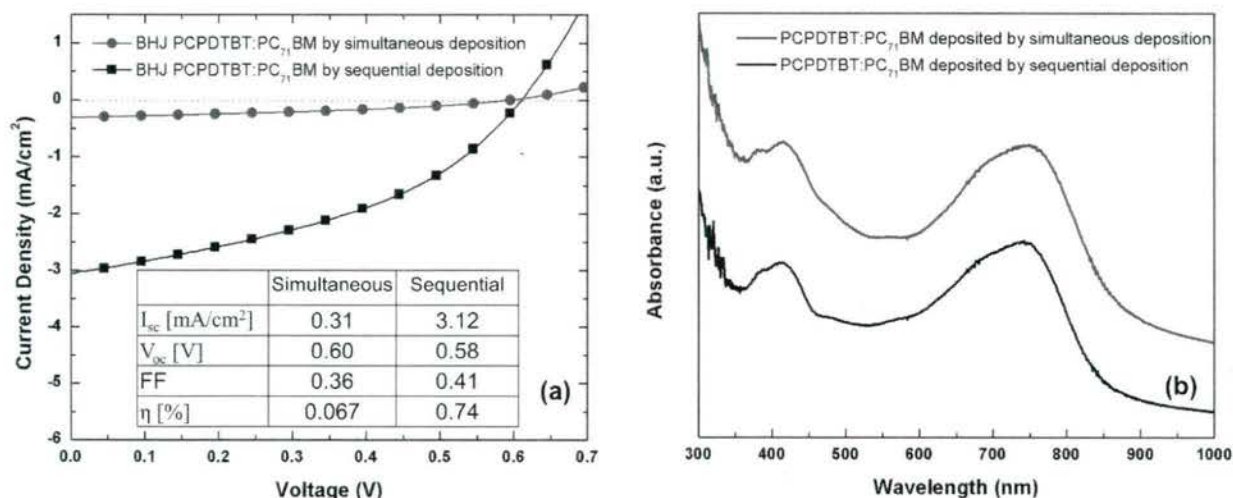


Figure 19. (a) J-V characteristics of PCPDTBT:PC<sub>71</sub>BM (1:1) BHJ OSCs fabricated by simultaneous (red) and sequential (black) deposition modes. The inset table is calculated performance parameters. (b) Stacked UV-Vis-NIR absorbance spectra of blended PCPDTBT:PC<sub>71</sub>BM (1:1) films deposited by simultaneous (red) and sequential (black) deposition modes.

### **Impact of Donor:Acceptor Ratio using Sequential Deposition Mode on Organic Solar Cells**

Having proven that the sequential deposition mode is most appropriate for the deposition of OSCs, and having identified the maximum surfactant concentration that can be used in the RIR-MAPLE emulsion targets, three BHJ material systems were



investigated: P3HT:PC<sub>61</sub>BM, PCPDTBT:PC<sub>71</sub>BM, and P3HT:CdSe CQDs. One of the important challenges to address for each of these material systems is to determine the best BHJ composition for thin films deposited by RIR-MAPLE. While the spin-casting process allows the user to directly determine the ratio of the two materials in the resultant film by solution concentration alone, the RIR-MAPLE process has an additional step that might be described as a “transfer efficiency.” For example, one prepared target may contain 1 wt% each of two separate materials dissolved and frozen within it resulting in a 1:1 volume ratio within the target. However, the rate at which the laser transfers each of the two materials to the substrate may be very different, depending on many factors, such as molecular weight, absorption coefficient of the emulsion, and the quality of the emulsion (i.e. oil/water domain sizes). Therefore, it is important to determine the optimum ratio of these materials *within the RIR-MAPLE target* in order to fabricate an optimized BHJ OPV. The following studies address this challenge for each of the material systems under investigation.

A systematic study of the effect of PCPDTBT:PC<sub>71</sub>BM BHJ ratio on the solar cell performance using the emulsion-based RIR-MAPLE sequential deposition mode was conducted. The BHJ ratio can be determined by the deposition growth rate for each material and the target partition ratio, as opposed to the weight ratio in solution typically used for solution-based methods. The UV-Vis-NIR absorbance spectra of PCPDTBT:PC<sub>71</sub>BM active regions with different BHJ ratios are shown in **Figure 20a**. As the ratio of PCPDTBT:PC<sub>71</sub>BM increases, that is, as the content of the polymer component increases in the BHJ, the PCPDTBT relative peak intensities increase, while the PC<sub>71</sub>BM relative peak intensities decrease. These trends demonstrate the ability to precisely control the BHJ ratio by emulsion-based RIR-MAPLE using sequential deposition. The J-V curves for the PCPDTBT:PC<sub>71</sub>BM BHJ OSCs with different ratios are shown in **Figure 20b**, and the corresponding device parameters are summarized in **Table 4**. The PCPDTBT:PC<sub>71</sub>BM BHJ ratio of 1:1.5 yielded the best device performance. From literature, the best ratio for the spin-coated PCPDTBT:PC<sub>71</sub>BM BHJ system is between 1:2 and 1:3.

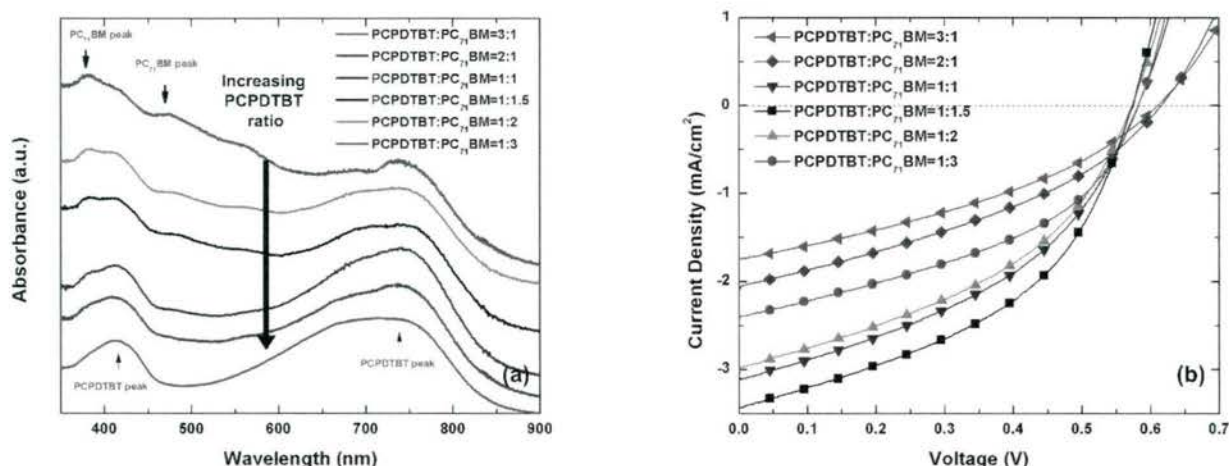


Figure 20. (a) Stacked UV-Vis-NIR absorbance spectra of PCPDTBT:PC<sub>71</sub>BM blended films with different ratios deposited by sequential deposition mode. The attribution of the peaks are highlighted by arrow marks. (b) The J-V curves of PCPDTBT:PC<sub>71</sub>BM BHJ OSCs deposited by sequential deposition mode.



Table 4. Performance of PCPDTBT:PC 71BM BHJ OSCs with different ratios fabricated by RIR-MAPLE using sequential deposition mode. The ratio of the two materials is indicated in parentheses (polymer: small molecule). All results were determined by averaging six devices.

BHJ Ratio	$J_{sc}$ (mA/cm <sup>2</sup> )	$V_{oc}$ (V)	FF	PCE (%)
(3:1)	1.76	0.61	0.36	0.39
(2:1)	2.05	0.62	0.36	0.46
(1:1)	3.12	0.58	0.41	0.74
(1:1.5)	3.43	0.56	0.45	0.86
(1:2)	2.99	0.57	0.42	0.72
(1:3)	2.40	0.58	0.43	0.60

Similarly, a wide range of P3HT:PC<sub>61</sub>BM volume ratios (in the target) was chosen for sequential deposition by RIR-MAPLE: 1:3, 1:2, 1:1, 2:1, 3:1. Calibration depositions of each material separately determined that P3HT tends to deposit nearly twice as fast as PCBM. Consequently, P3HT was prepared at a reduced concentration in its primary solvent, ortho-dichlorobenzene (oDCB), compared to PCBM in its primary solvent (also oDCB) as an attempt to equalize the deposition rates. The RIR-MAPLE target was partitioned so that each material is frozen separately in its own location and can therefore be used to control the ratio of the materials in the film. For each P3HT:PC<sub>61</sub>BM ratio, six 9 mm<sup>2</sup> OSC devices per substrate were measured separately for the J-V and external quantum efficiency (EQE) measurements. The average current density versus applied bias is shown in **Figure 21**, with the corresponding device metrics shown in **Table 5**. The device with the highest power conversion efficiency (PCE) was the 1:1 ratio device with PCE = 0.725%.

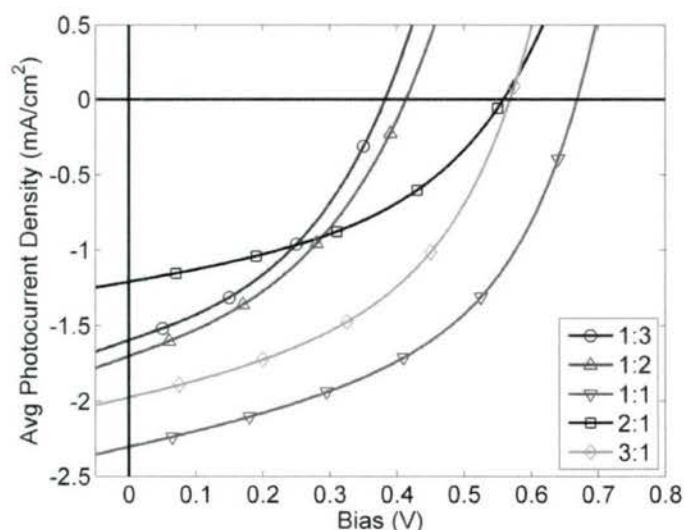


Figure 21. Average photocurrent density versus applied bias for each of the five RIR-MAPLE target volume ratios: 1:3, 1:2, 1:1, 2:1, and 3:1. Each curve is the average of six different 9 mm<sup>2</sup> devices.

Table 5. OPV metrics for the P3HT:PCBM BHJ ratio study.

P3HT:PCBM	V <sub>oc</sub> (V)	J <sub>sc</sub> (mA/cm <sup>2</sup> )	FF	PCE (%)
1:3	0.383	1.594	0.396	0.242
1:2	0.414	1.701	0.388	0.273
1:1	0.670	2.303	0.469	0.725
2:1	0.560	1.209	0.417	0.282
3:1	0.569	1.973	0.444	0.499

The results of the initial ratio study indicated that a 1:1 P3HT:PC<sub>61</sub>BM BHJ ratio in the RIR-MAPLE target would give the optimal results for a BHJ OSC. However, spin-cast films tend to exhibit their optimal performance at a ratio of P3HT:PC<sub>61</sub>BM slightly larger than unity, such as 1:0.7 or 1:0.8. Therefore, an extension of the ratio study was made to the region around 1:1. Three ratios were chosen: 0.7:1, 1:1, and 1:0.7. These ratios represent the volume of each material present in the RIR-MAPLE target. The emulsion targets for each material were prepared identically to those prepared for the first ratio study. The results of this optimization study are shown in the J-V curves of **Figure 22** and the corresponding device metrics are shown in **Table 6**. Surprisingly, the optimum RIR-MAPLE ratio was found to be the opposite of spin-cast films at 0.7:1 P3HT:PC<sub>61</sub>BM by volume. This ratio also provided the best performing devices with an average PCE ~ 1.0%.

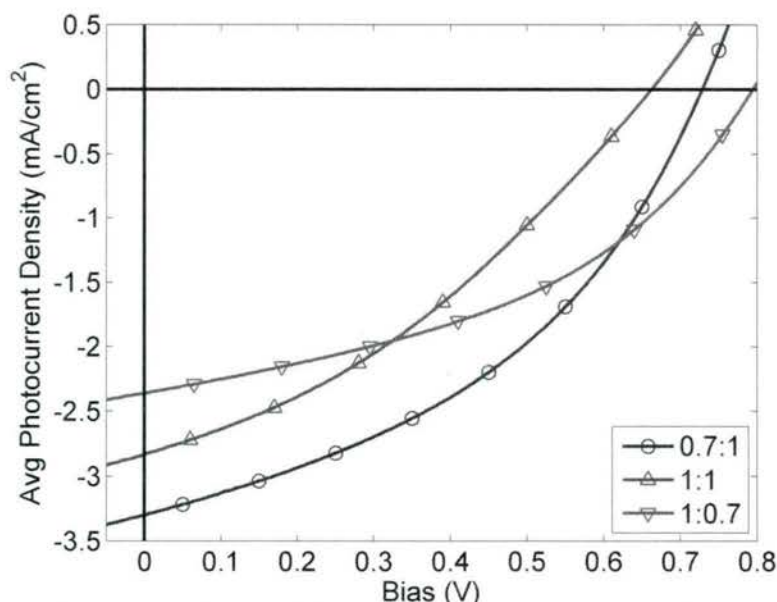


Figure 22. Average J-V characteristics of the 2nd ratio study to determine the true optimum RIR-MAPLE target ratio of P3HT:PC<sub>61</sub>BM in a BHJ OPV device. Each curve is the average of six different 9 mm<sup>2</sup> devices. The work was motivated by knowledge of the optimum ratio of P3HT:PCBM in spin-cast films, which is slightly larger than unity.



Table 6. OPV metrics for the P3HT:PC61BM BHJ ratio study near 1:1.

P3HT:PC <sub>61</sub> BM	V <sub>oc</sub> (V)	J <sub>sc</sub> (mA/cm <sup>2</sup> )	FF	PCE (%)
0.7:1	0.735	3.278	0.415	0.998
1:1	0.663	2.806	0.344	0.640
1:0.7	0.794	2.361	0.429	0.804

### **Impact of Emulsion Target Primary Solvent on Organic Solar Cells**

The impact of the primary solvent used in the RIR-MAPLE target on the thin film properties and OSC device performance was investigated in this work. Two families of organic solvents were used as the primary solvent in the emulsion targets used for RIR-MAPLE. In alkyl aromatic solvents, the three solvents considered include methylbenzene, 1,2-dimethylbenzene and 1,2,4-trimethylbenzene. These three solvents are commonly known as toluene, oxylene, and pseudocumene, respectively. In chlorinated aromatic solvents, the three solvents under study are chlorobenzene (CB), 1,2-dichlorobenzene (ODCB) and 1,2,4-trichlorobenzene (TCB). Atomic force microscopy (AFM) is used to characterize film surface morphology. The current density-voltage (J-V) power conversion efficiency measurements are used to characterize device performance.

**Figure 23** shows the AFM height images of the PCPDTBT thin films deposited from different chlorinated aromatic solvents (CB, ODCB, TCB) in both 25µm x 25µm and 5µm x 5µm scan sizes (RMS surface roughness value, R<sub>q</sub>, shown as inset in each image). Within the family of chlorinated aromatic solvents, the RMS surface roughness and the lateral size of surface features decrease from CB to ODCB to TCB. The smoothest PCPDTBT film is deposited from TCB, which has an RMS surface roughness value (R<sub>q</sub>) of 16.1nm on a 25µm x 25µm scan size.

To fabricate the BHJ OSCs using RIR-MAPLE with different primary solvents, sequential deposition mode is used. The PCPDTBT emulsion comprised different primary solvents, and the PC<sub>71</sub>BM emulsion used ODCB was used as the primary solvent. The same emulsion recipe was used for PC<sub>71</sub>BM deposition in all OSCs so that only the influence of the PCPDTBT deposition on the performance of solar cells was considered. The measured J-V curves of the OSCs deposited from these different solvents are shown in **Figure 24**, and the measured device parameters are listed in **Table 7**. As can be seen, the OSC deposited from TCB shows the best efficiency around 1.2%, followed by ODCB and CB. Toluene yields the solar cell with the poorest efficiency, only around 0.16%, which is one order magnitude lower than the OSC fabricated from TCB.

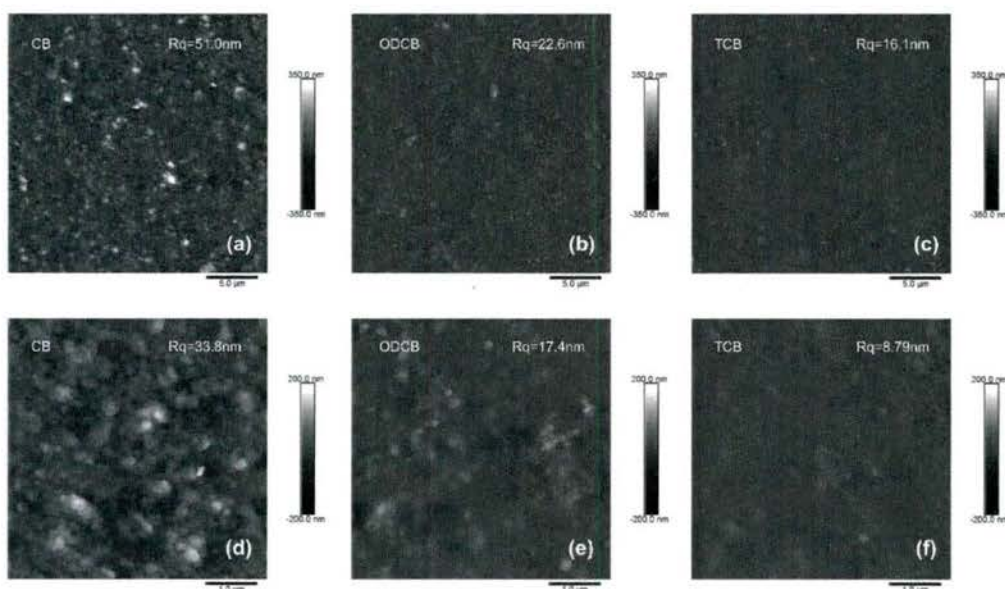


Figure 23. AFM height images of PCPDTBT films deposited from chlorobenzene, 1,2-dichlorobenzene, and 1,2,4-trichlorobenzene.

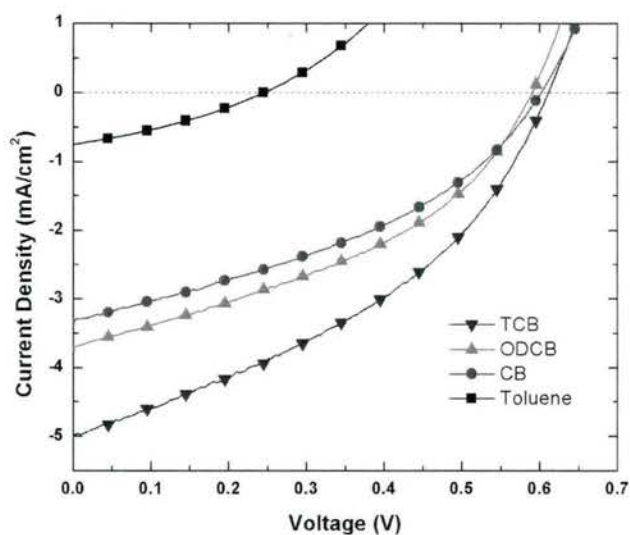


Figure 24. The J-V curves of PCPDTBT:PC71BM BHJ OSCs (1:1.5) deposited by RIR-MAPLE using different primary solvents for PCPDTBT target emulsion.

Table 7. Performance of PCPDTBT:PC 71BM BHJ OSCs (1:1.5) desposited by RIR-MAPLE using different primary solvents for PCPDTBT target emulsion. The results are averaged by six devices.

Primary Solvent	$J_{sc}$ (mA/cm <sup>2</sup> )	$V_{oc}$ (V)	FF	PCE (%)
Toluene	1.01	0.445	0.366	0.165
Chlorobenzene	3.33	0.600	0.385	0.770
1,2-Dichlorobenzene	3.70	0.590	0.400	0.872
1,2,4- Trichlorobenzene	5.00	0.610	0.392	1.196



A similar study was performed for the P3HT:PCBM material system. **Figure 25** shows the AFM height images of the P3HT:PCBM thin films deposited from the set of six primary solvents (RMS surface roughness value,  $R_q$ , shown as inset in each image). The smoothest film is deposited from TCB, which has an RMS surface roughness value ( $R_q$ ) of 11.0nm on a  $25\mu\text{m} \times 25\mu\text{m}$  scan size. The measured J-V curves of the OSCs deposited from these different solvents are shown in **Figure 26**, and the measured device parameters are listed in **Table 8**. As can be seen, the OSC deposited from TCB shows the best efficiency around 3.3%, followed by ODCB and CB. Toluene yields the solar cell with the poorest efficiency, around 1.84%.

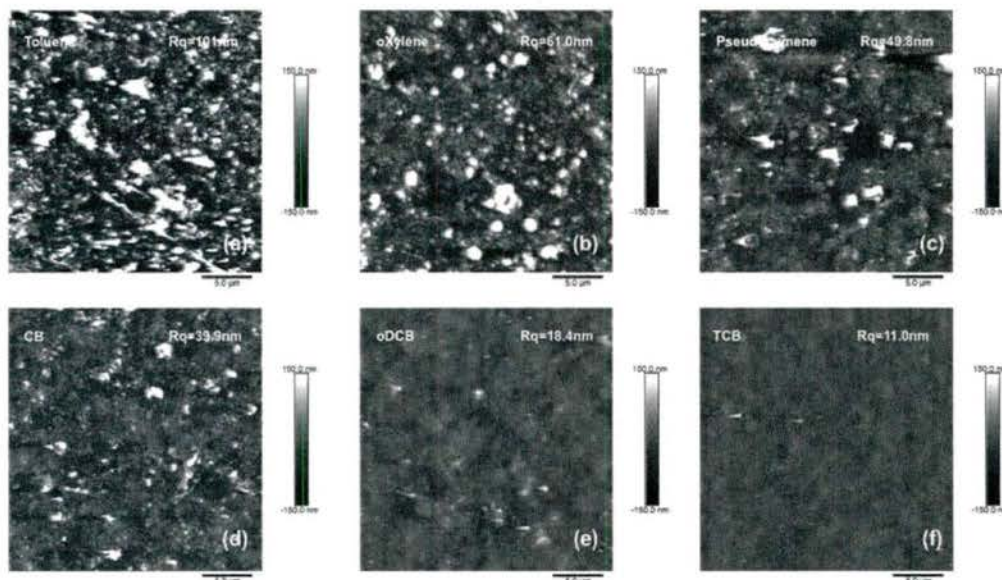


Figure 25. AFM height images of P3HT:PCBM films deposited from the six primary solvents.

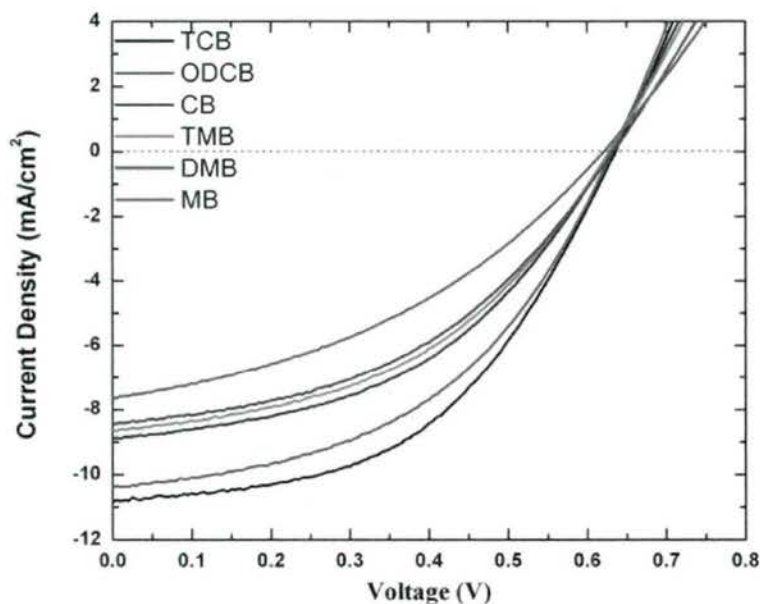


Figure 26. The J-V curves of P3HT:PC61BM BHJ OSCs (1:1.5) deposited by RIR-MAPLE using different primary solvents for P3HT target emulsion.

Table 8. Performance of P3HT:PC 61BM BHJ OSCs (1:1.5) desposited by RIR-MAPLE using different primary solvents for P3HT target emulsion. The results are averaged by six devices.

Primary solvent	Voc (V)	Jsc(mA/cm <sup>2</sup> )	FF	PCE (%)
TCB	0.63 (0.0041)	10.62(0.27)	0.488(0.011)	3.27(0.079)
ODCB	0.64(0.0024)	10.47(0.10)	0.448(0.014)	2.99(0.084)
CB	0.63(0.035)	8.85(0.026)	0.4535(0.043)	2.51(0.043)
TMB	0.63(0.0025)	8.58(0.15)	0.445(0.0052)	2.42(0.038)
DMB	0.63(0.0035)	8.33(0.10)	0.393(0.0060)	2.06(0.027)
MB	0.61(0.0094)	7.79(0.15)	0.387(0.0061)	1.84(0.081)

### Impact of Percolation Threshold on Hybrid Nanocomposite Solar Cells

The fabrication of PCPDTBT-CdSe hybrid organic cells starts with optimizing the CdSe loading in the blended film. By tuning the CdSe target volume ratio in the entire target, the CdSe loading can be controlled. The J-V curve of RIR-MAPLE fabricated PCPDTBT-CdSe hybrid organic solar cell with different CdSe loading are shown in **Figure 27a**. The measured and calculated device parameters are listed in the **Table 9**. As can be seen, the performance of the solar cells strongly depends on the CdSe loading, and 80% CdSe device yields the best device performance, which is around 0.4%. **Figure 27b** shows the external quantum efficiency (EQE) of the hybrid solar cells with different CdSe loading. As can be seen, the EQE spectra extend to 900nm, which is due to the NIR light absorption from the low band gap polymer PCPDTBT. The peak between 600-650 nm is attributed to CdSe nanoparticle absorption and becomes pronounced when the CdSe loading reaches to 80% or higher. The EQE measurement demonstrates both PCPDTBT and CdSe contribute to photocurrent and RIR-MAPLE effectively blend the PCPDTBT and CdSe together, which effectively work as solar cells. Despite that the hybrid solar cells fabricated by RIR-MAPLE exhibit clear photovoltaic effect, the efficiency of the devices are lower than typical ones fabricated by spin-casting. One possible explanation of the low efficiency is the presence of excess surfactant – 0.005 wt% SDS is necessary to stabilize CdSe emulsion, in contrast to the PCPDTBT emulsion target that only requires 0.001wt% SDS.

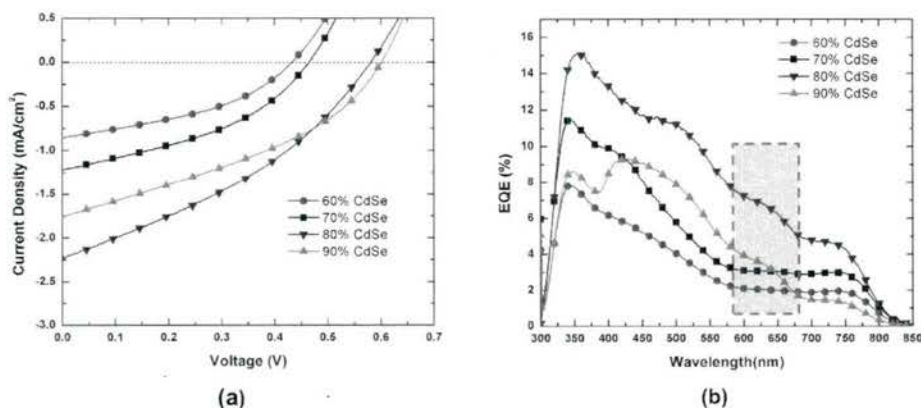


Figure 27. (a) J-V curve of PCPDTBT-pyridine CdSe hybrid organic solar cell fabricated by RIR-MAPLE; and (b) EQE spectra of the corresponding solar cells with different CdSe loading.



Table 9. Summary of photovoltaic performance under one sun AM 1.5 G illumination for PCPDTBT- pyridine CdSe hybrid organic solar cells fabricated by RIR-MAPLE with different CdSe loading.

CdSe loading	$J_{sc}$ (mA/cm <sup>2</sup> )	$V_{oc}$ (mV)	Fill factor, FF (%)	PCE (%)
60%	0.77±0.06	418.3±21.1	39.7±0.7	0.13±0.02
70%	1.21±0.02	463.3±2.58	39.9±0.2	0.22±0.03
80%	2.04±0.20	567.5±8.80	35.3±0.1	0.41±0.04
90%	1.61±0.14	595.0±5.78	36.6±0.2	0.35±0.03

### Impact of Tandem Active Regions on Organic Solar Cells

RIR-MAPLE was used to fabricate tandem OSCs for the first time. The general tandem structure deposited by RIR-MAPLE is shown schematically in **Figure 28**, and uses two different BHJ active regions that are sensitive to different regions of the solar spectrum. Different tunnel junction configurations, some uniquely enabled by RIR-MAPLE, were attempted: titanium oxide (TiO<sub>x</sub>) nanoparticles, PEDOT:PSS, blend of TiO<sub>x</sub> nanoparticles and PEDOT:PSS, as well as no tunnel junction between the two active regions. As shown in **Figure 29** and **Table 10**, the best performing tandem device occurred for the tunnel junction using a blend of TiO<sub>x</sub> nanoparticles and PEDOT:PSS. The main reason for the better performance compared to other tandem structures is that the open circuit voltages increased as expected for two solar cell active regions in series. While more work is required to optimize the growth of tandem structures using emulsion-based RIR-MAPLE, these results are important in that they demonstrate the capability to explore a wider range of tunnel junction materials due to the limited influence of solvents on the device structures that can be grown.

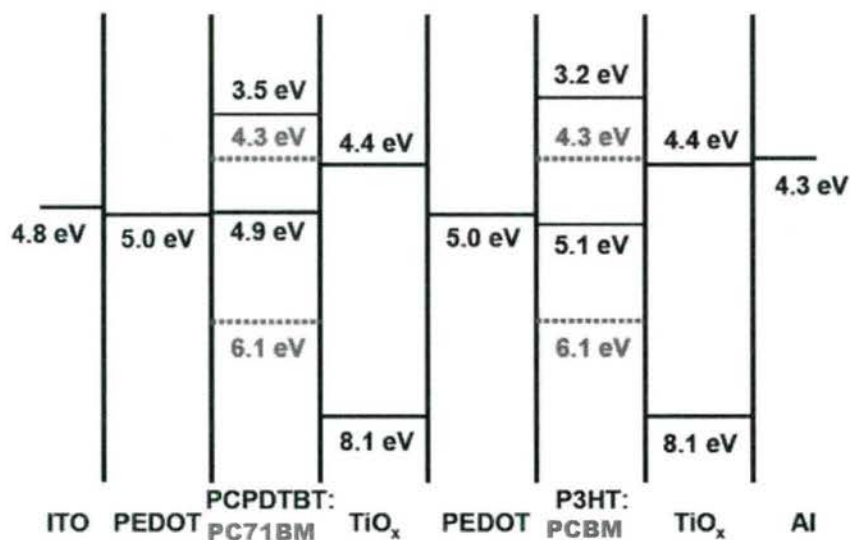


Figure 28. Energy band diagram for PCPDTBT-PC71BM organic solar cells fabricated by RIR-MAPLE with different tandem structures.

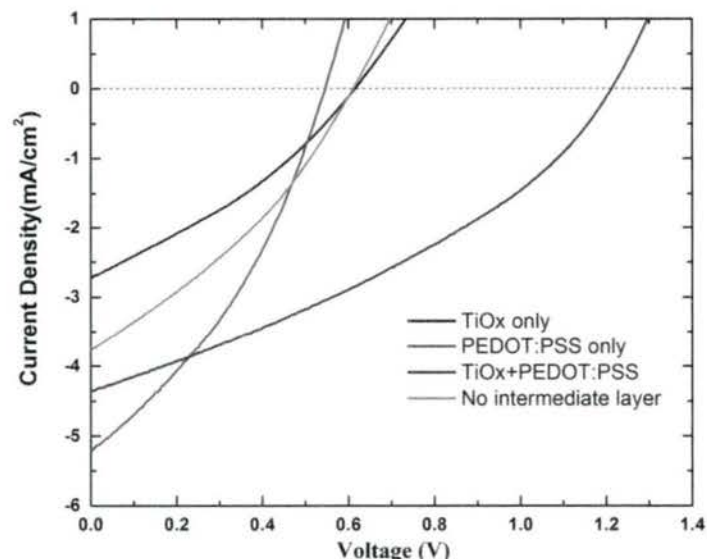


Figure 29. J-V curves of PCPDTBT-PC71BM organic solar cells fabricated by RIR-MAPLE with different tandem structures.

Table 10. Summary of photovoltaic performance under one sun AM 1.5 G illumination for tandem and ternary organic solar cells fabricated by RIR-MAPLE.

Active Region Structure	Voc (V)	Jsc(mA/cm2)	FF	PCE (%)
Tandem TiOx only	0.62	3.60	0.348	0.77
Tandem PEDOT only	0.54	5.20	0.353	1.00
With both TiOx and PEDOT	1.21	4.22	0.338	1.73
No Intermediate layer	0.61	3.77	0.331	0.76

#### 4.4 Simulation Tool for Optoelectronic Device Performance in Thin Films Deposited by RIR-MAPLE

##### Semi-Empirical Dynamic Monte Carlo Model of Organic Solar Cells

One unique aspect of the DMC model developed in this work is that the BHJ donor and acceptor domains were represented by the two-dimensional (2D), microscale average feature size determined by confocal microscopy images. This approach has been used to investigate the impact of BHJ polymer ratio on the device performance of organic solar cells deposited by RIR-MAPLE using the sequential deposition mode. Following a semi-empirical approach, grazing incidence, wide-angle X-ray scattering (GI-WAXS) was used to measure the thin film structure for the RIR-MAPLE deposited thin films with different BHJ compositions. The measured structure was quantified by the proportion of  $\pi$ - $\pi$  stacking in the out-of-plane and in-plane directions, as well as the corresponding, measured value of the lattice constant. These parameters served as input to the DMC model in order to predict the external quantum efficiency.

As demonstrated in the microscopy images of P3HT-PC<sub>61</sub>BM BHJs shown in **Figure 30**, the average feature size in the image varies as a function of the BHJ polymer ratio



(polymer:small molecule). In these images, the red regions represent the polymer, and the black regions represent the small molecule. The 2D average feature sizes for P3HT:PC<sub>61</sub>BM BHJs with different polymer ratios 1:1, 2:1, and 3:1 are 6.82  $\mu\text{m}$ , 11.5  $\mu\text{m}$ , and 14.0  $\mu\text{m}$ , respectively (analysis performed on minimum of 40 images for each sample).

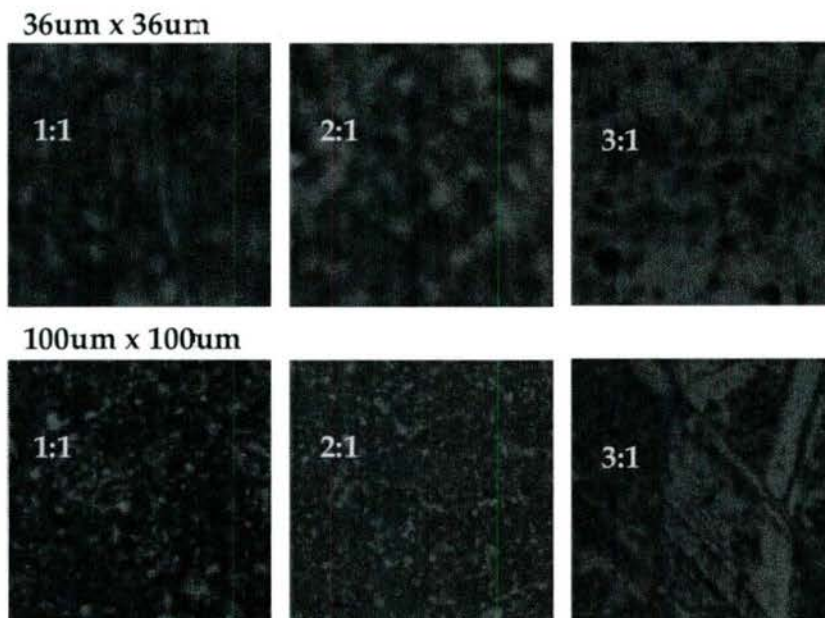


Figure 30. Zeiss LSM 510 confocal microscope images for RIR-MAPLE P3HT:PC<sub>61</sub>BM BHJs of different ratios: 1:1, 2:1, and 3:1 showing the structural changes in features on two different size scales: (1) 36 x 36 $\mu\text{m}$ ; (2) 100 x 100 $\mu\text{m}$ . The red regions represent the polymer, while the black regions represent the small molecule.

**Figure 31** shows the 2D GI-WAXS plots for scattering data from the RIR-MAPLE-deposited BHJs with different polymer ratios, along with data from P3HT-only and PC<sub>61</sub>BM-only samples. Integrating the intensities in a direction perpendicular to the substrate (z-direction) gives a one-dimensional (1D) out-of-plane OOP GI-WAXS scattering profile, while integration along the direction of the substrate (xy-direction) gives the corresponding in-plane (P) GI-WAXS profile, as shown in **Figure 32**. The relative peak intensities for  $\pi$ - $\pi$  stacking (corresponding to the (010) peak) compared to the (100) peak representing lamellar stacking are used to quantify the occurrence of the higher mobility charge transport in the out-of-plane and in-plane directions. The corresponding q-values of these peaks are directly linked to the material lattice constant (the d-value), and are also used in the charge transport DMC simulation. We have used this model to simulate different active region morphologies for testing against the experimental results, namely BHJ, bi-layer, and graded structures, as shown in **Figure 33**.

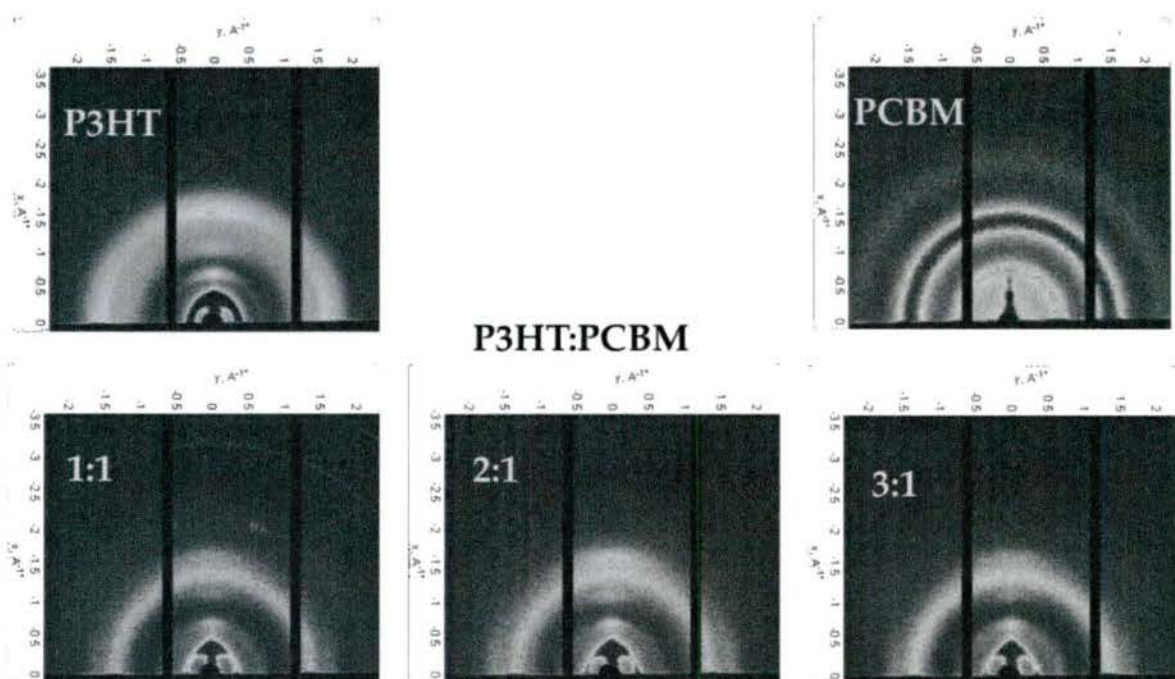


Figure 31. GI-WAXS images of 2D scattering intensity for RIR-MAPLE P3HT:PC61BM BHJs of different ratios. Images for RIR-MAPLE P3HT- and PC61BM-alone samples are included for comparison.

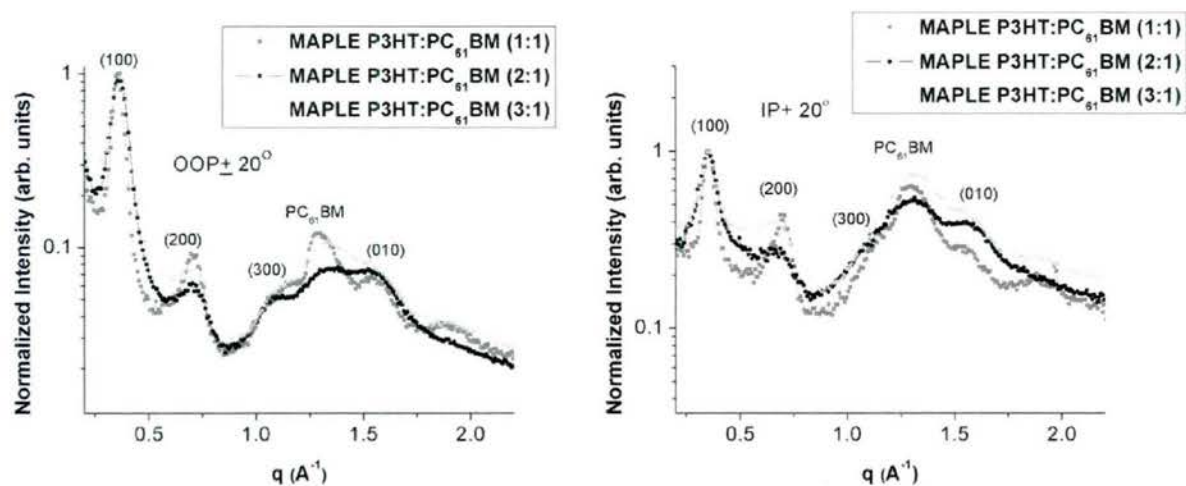


Figure 32. 1D GI-WAXS scattering profiles obtained from Figure 3 by integration along the (a) out-of-plane (OOP) and (b) in-plane (IP) directions, and normalized to the P3HT (100) peak around  $q=0.3\text{\AA}^{-1}$ .



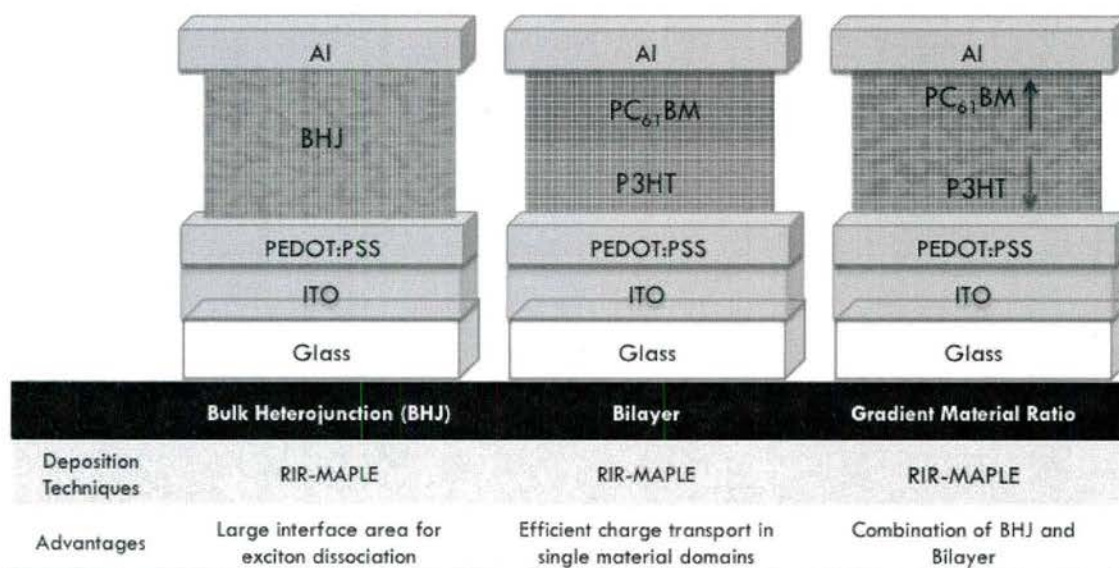


Figure 33. Schematic diagrams of the different P3HT:PC61BM OPV heterostructures fabricated using RIR-MAPLE.

In the graded structure, the active region film composition varies gradually from pure P3HT at the substrate surface to pure PC<sub>61</sub>BM at the film surface; yet, confirmation of the gradient composition in the graded active is needed for testing the simulated results against the experimental device performance. Thus, X-ray photoelectron spectroscopy (XPS), and the sputtering capability of the system, were used to verify that the graded structure existed in the film deposited by RIR-MAPLE. The sputtering was performed using an Argon Ion gun turned on for 60s each cycle with 50s wait times before chemical analysis was done. Thus, the sputtering time serves as a direct analog to the depth within the film from the film surface to the substrate surface. The peaks of interest are: C 1s at 284.4eV, which includes some carbon from P3HT (C<sub>10</sub>H<sub>14</sub>S)<sub>n</sub> but is dominated by PC<sub>61</sub>BM (C<sub>72</sub>H<sub>14</sub>O<sub>2</sub>); S 2p centered around 165eV, representing sulfur that is present only in the polymer material; and O 1s near 529eV. **Figure 34** shows the relative atomic concentration for the BHJ and graded active region structures. While the BHJ S 2p composition (from P3HT) ranges from 2% to 5% after 2400secs of sputtering, the graded film S 2p composition jumps from 2% to almost 30% within the same sputtering time. Also, the rise in the S 2p concentration from P3HT with increasing depth (red squares) is matched by a reduction in the C 1s concentration (red stars), primarily from PC61BM. This depth profile of composition provides evidence that the RIR-MAPLE growth did achieve a graded structure. In **Figure 35**, the simulated external quantum efficiency (EQE) spectra for the different active region structures are shown. The best performance occurs for the graded active region (reaching a maximum EQE of about 15%), which is expected because it combines the favorable microscale properties of the BHJ and bilayer.

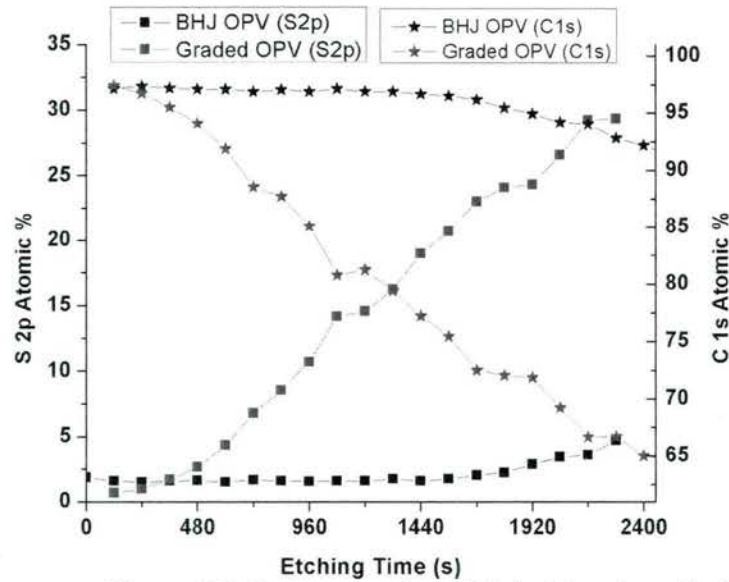


Figure 34. Atomic compositions of S 2p (squares) and C 1s (stars) peaks for P3HT:PC61BM BHJ (black lines) and graded (red lines) active regions with increasing etching times to provide a compositional depth profile of the films.

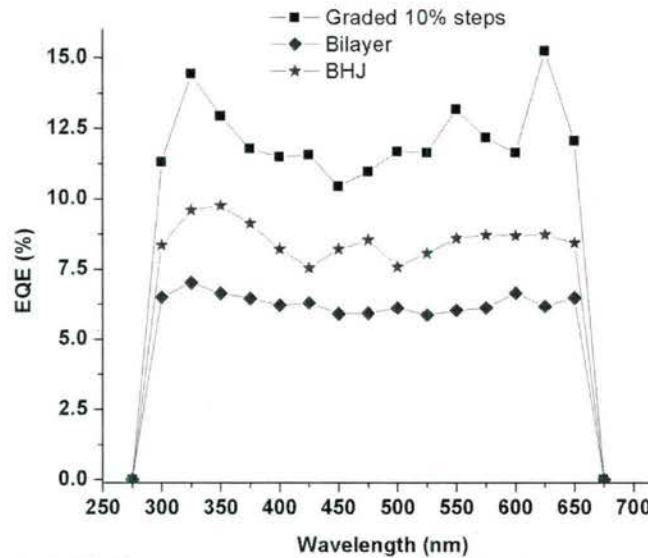


Figure 35. Simulated EQE spectra using microscale DMC model comparing different P3HT:PC61BM active region structures.

**Figure 36** compares the microscale DMC results with measured data for P3HT:PC<sub>61</sub>BM OSC devices fabricated by RIR-MAPLE with the same morphologies. It appears as though the microscale DMC model most accurately simulates the graded OPV system, where the simulated EQE (~ 12-15 %) is much closer to the experimentally determined values and the short circuit current density approaches the experimental values determined from two different experimental techniques (2.4mA/cm<sup>2</sup> for the DMC, 3.1mA/cm<sup>2</sup> from the J-V curve, and 2.9mA/cm<sup>2</sup> from integrating the measured EQE spectrum).



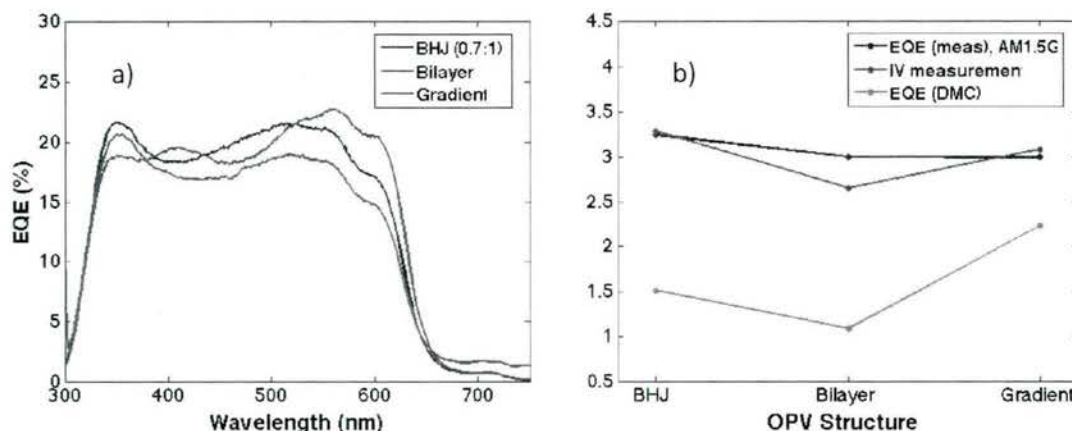


Figure 36. (a) Measured EQE spectra and (b) Jsc from measured EQE spectra, J-V data, and simulated EQE for the three active region structures of P3HT:PC61BM OPVs: BHJ, bilayer, and graded.

## 5.0 CONCLUSIONS

A main goal of this work has been to establish the relationships among RIR-MAPLE growth parameters (especially target emulsion recipe), thin-film structure and material properties, and device performance. CQDs, which are less viscous than polymers, tend to stay in the solvent and aggregate as the solution dries. This eventually results in the formation of CQD aggregates in the areas of the substrate where the solvent evaporates more slowly. In contrast, we show that emulsion-based RIR-MAPLE using the sequential deposition mode improves the dispersion of CQDs in conjugated polymers by minimizing the solvent evaporation process. Thus, RIR-MAPLE deposition of hybrid nanocomposites is fundamentally different from solution processed deposition techniques and reduces nanoparticle phase segregation by: i) eliminating the need to co-dissolve nanoparticles and polymers into a single common solvent by using the sequential deposition mode; and ii) depositing the nanoparticles and polymers in a relatively dry state. In addition, RIR-MAPLE provides a facile way to deposit thin films on a large scale with good control of uniformity and little to no requirements of the substrate materials.

TOF mobility measurements were used to demonstrate the important advantage of RIR-MAPLE deposition, compared to traditional solution-based techniques (such as drop-casting and spin-casting), with regard to increasing the hole drift mobility (vertical transport) in conjugated polymer films. This work demonstrated that RIR-MAPLE-deposited MEH-PPV films offer an enhanced hole mobility ( $6.0 \times 10^{-6} \text{ cm}^2/\text{Vs}$  at  $25^\circ\text{C}$  and  $2.5 \times 10^5 \text{ V/cm}$ ), in comparison to drop-cast ( $2.5 \times 10^{-6} \text{ cm}^2/\text{Vs}$  at  $25^\circ\text{C}$  and  $2.5 \times 10^5 \text{ V/cm}$ ) and spin-cast ( $1.1 \times 10^{-6} \text{ cm}^2/\text{Vs}$  at  $25^\circ\text{C}$  and  $2.5 \times 10^5 \text{ V/cm}$ ) MEH-PPV films, due to more relaxed polymer chains. Also, RIR-MAPLE enabled a modified TOF measurement technique appropriate for hybrid nanocomposites (CdSe CQDs embedded in MEH-PPV). This study provided the important insight that the percolation threshold in bulk heterojunction solar cells using CQDs deposited by RIR-MAPLE required a smaller concentration of CQDs, which means that the device fabrication process can be less wasteful compared to solution processing of hybrid nanocomposites.

A model to determine the infrared, intraband absorption coefficient in polymer-nanoparticle hybrid nanocomposites was developed and experimentally verified.



Importantly, this model explicitly included the influence of organic surface ligands such that the impact of surface ligand exchange and removal can be considered as a design parameter for infrared photodetectors. The *in-situ* polymerization of a third monomer source [2-aminoethyl methacrylate hydrochloride (AEM)] in polymer-CQD hybrid nanocomposites [blend of ligand-capped CdSe CQDs and MEH-CN-PPV] was demonstrated as a technique to promote better charge transfer between the constituent polymer and nanoparticle materials. In addition, a multi-spectral (visible and IR) hybrid nanocomposite photodetector enabled by the RIR-MAPLE deposition using the *in-situ* polymerization technique was demonstrated. The device operated at room temperature and provided high responsivity ( $\sim 10$  A/W) at low bias ( $< +2$  V).

Three BHJ material systems have been used to determine the impact of RIR-MAPLE on the thin film properties and corresponding OSC device performance: P3HT:PC<sub>61</sub>BM, P3HT:CdSe CQDs, and PCPDTBT:PC<sub>71</sub>BM. Although the RIR-MAPLE solar cell device performance is not comparable to the efficiencies currently achievable with spin-coating, it has been demonstrated that: i) the sequential deposition mode is best suited to organic solar cell (OSC) deposition by RIR-MAPLE; ii) the maximum amount of surfactant that can be included in the RIR-MAPLE target is 0.001wt% in DI water; and iii) the optimized BHJ composition for thin films deposited by RIR-MAPLE differ from those achieved using solution processing. The OSC device demonstrations using RIR-MAPLE for the active region deposition represent an improvement by 1-2 orders of magnitude from the first UV MAPLE-deposited OSC (PCE = 0.03% for OSC with a bilayer active region).

Finally, with regard to controlling polymer and nanocomposite film morphology for enhanced charge transport, we developed a simulation tool using a Dynamic Monte Carlo algorithm to relate the morphology of RIR-MAPLE deposited films to optoelectronic device performance, especially solar cells and photodetectors. The simulation tool consists of three parts: i) an algorithm to generate the BHJ morphologies, ii) a transfer matrix calculation to determine the exciton generation rate and spatial distribution, and iii) a Dynamic Monte Carlo (DMC) model to simulate charge transport within the organic solar cell. The simulation tool uses measured material properties as input, and the output includes external quantum efficiency spectra that can be compared directly to measured devices. The simulations have been compared to experimental results, demonstrating a useful approach to explore optoelectronic device design and RIR-MAPLE growth.



## APPENDIX A – LIST OF PUBLICATIONS

1. K. R. Lantz and A. D. Stiff-Roberts, "Theoretical Investigation of Intraband, Infrared Absorbance in Inorganic/Organic Nanocomposite Thin Films with Varying Colloidal Quantum Dot Surface Ligand Materials," Lester Eastman Conference on High Performance Devices, Troy, NY, August 2010.
2. R. McCormick, A. D. Stiff-Roberts, and J. Lenhardt, "Matrix-Assisted Pulsed Laser Evaporation of Organic Materials for Optoelectronic Devices," Materials Research Society Fall Meeting, Boston, MA, December 2010.
3. A. D. Stiff-Roberts, "Quantum dot infrared photodetectors," in Comprehensive Semiconductor Science and Technology, vol. 6, pp. 452-485, Edited by P. Bhattacharya, R. Fornari, and H. Kamimura, Elsevier, Amsterdam (2011).
4. A. D. Stiff-Roberts, "Colloidal Quantum Dot-Conducting Polymer Nanocomposites for Multi-spectral Photodetection," Fitzpatrick Institute for Photonics Annual Meeting, Durham, NC, October 2011.
5. R. Pate, R. McCormick, L. Chen, W. Zhou, and A. D. Stiff-Roberts, "RIR-MAPLE Deposition of Conjugated Polymers for Application to Optoelectronic Devices," (INVITED) Applied Physics A: Materials Science and Processing, vol. 105, pp. 555-563, November 2011 (DOI 10.1007/s00339-011-6598-3).
6. K. R. Lantz and A. D. Stiff-Roberts, "Calculation of Intraband Absorption Coefficients in Organic/Inorganic Nanocomposites: Effects of Colloidal Quantum Dot Surface Ligand and Dot Size," IEEE Journal of Quantum Electronics, vol. 47, pp. 1420-1427, November 2011.
7. R. Pate and A. D. Stiff-Roberts, "Influence of Semiconductor Nanocrystal Concentration on Polymer Hole Transport in Hybrid Nanocomposites," Crystals, vol. 2, pp. 78-89, January 2012.
8. R. McCormick, J. Lenhardt, and A. D. Stiff-Roberts, "Effects of emulsion-based resonant infrared matrix assisted pulsed laser evaporation (RIR-MAPLE) on the molecular weight of polymers," Polymers, vol. 4, pp. 341-354, February 2012.
9. A. D. Stiff-Roberts, "Emulsion-Based Resonant Infrared Matrix-Assisted Pulsed Laser Evaporation: An Enabling Technology for Organic-Based Optoelectronic Devices," Center for Metamaterials and Integrated Plasmonics (CMIP) Seminar Series, Duke University, Durham, NC, February 2012.
10. A. D. Stiff-Roberts, R. Pate, R. McCormick, and K. Lantz, "RIR-MAPLE Deposition of Conjugated Polymers and Hybrid Nanocomposites for Application to Optoelectronic Devices," (INVITED) International High-Power Laser Ablation Conference, Santa Fe, NM, April 2012.
11. A. D. Stiff-Roberts, "Emulsion-Based Resonant Infrared Matrix-Assisted Pulsed Laser Evaporation: An Enabling Technology for Organic-Based Optoelectronic Devices," Materials Science and Engineering Distinguished Colloquium Speaker Series, Northwestern University, Evanston, IL, April 2012.



12. Y. Park and A. D. Stiff-Roberts, "In situ Polymerization of CdSe/MEH-CN-PPV Inorganic Nanoparticle/Polymer Composites for High-Responsivity, Thin Film Photodetectors," Materials Research Society Spring Meeting, San Francisco, CA, April 2012.
13. A. D. Stiff-Roberts, R. Pate, R. McCormick, and K. R. Lantz, "RIR-MAPLE deposition of conjugated polymers and hybrid nanocomposites for application to optoelectronic devices," (INVITED) AIP Conference Proceedings (International Symposium on High Power Laser Ablation), vol. 1464, pp. 347-357, May 2012.
14. Y. Park, J. Park, M. J. Therien, and A. D. Stiff-Roberts, "Enhanced Dispersion of CdSe/MEH-CN-PPV Hybrid Nanocomposites by in situ Polymerization using AEM as Photopolymerizable Precursor," Colloid and Polymer Science, vol. 290, pp. 1501-1509, May 2012.
15. A. Atewologun, W. Ge, and A. D. Stiff-Roberts, "Characterization of Colloidal Quantum Dot Ligand Exchange and Removal by X-ray Photoelectron Spectroscopy," Electronic Materials Conference, State College, PA, June 2012.
16. A. D. Stiff-Roberts, "Hybrid Nanocomposite Infrared Photodetectors," (INVITED) 11th International Conference on Infrared Optoelectronics: Materials and Devices (MIOMD-XI), Evanston, IL, September 2012.
17. A. D. Stiff-Roberts and R. D. McCormick, "Resonant Infrared Matrix-Assisted Pulsed Laser Evaporation of P3HT-based Bulk Heterojunctions: Small-Angle X-ray Scattering and Photovoltaic Device Characterization," ORNL CNMS User Meeting, Oak Ridge, TN, September 2012 (poster).
18. A. D. Stiff-Roberts, "Emulsion-Based Resonant Infrared Matrix-Assisted Pulsed Laser Evaporation: An Enabling Technology for Organic-Based Optoelectronic Devices," Joint School of Nanoscience and Nanoengineering (JSNN) Seminar Series, JSNN, Greensboro, NC, November 2012.
19. A. D. Stiff-Roberts, "Emulsion-Based Resonant Infrared Matrix-Assisted Pulsed Laser Evaporation: An Enabling Technology for Organic Optoelectronic Devices," (INVITED) Energy Materials Nanotechnology (EMN) West Meeting, Houston, TX, January 2013.
20. A. D. Stiff-Roberts, R. D. McCormick, and K. Xiao, "Enhancement of vertical charge transport in organic photovoltaic devices deposited by resonant infrared matrix-assisted pulsed laser evaporation (RIR-MAPLE)," Fitzpatrick Institute for Photonics Annual Meeting, Durham, NC, March 2013.
21. A. Atewologun, W. Ge, and A. D. Stiff-Roberts, "Characterization of Colloidal Quantum Dot Ligand Exchange by X-ray Photoelectron Spectroscopy," Journal of Electronic Materials, vol. 42, pp. 809-814, May 2013.
22. R. D. McCormick, K. Xiao, A. Payzant, and A. D. Stiff-Roberts, "Enhancement of vertical charge transport in organic photovoltaic devices deposited by resonant infrared matrix-assisted pulsed laser evaporation (RIR-MAPLE)," Electronic Materials Conference, South Bend, IN, June 2013.



23. A. D. Stiff-Roberts, "Emulsion-Based Resonant Infrared Matrix-Assisted Pulsed Laser Evaporation: An Enabling Technology for Organic Thin Films," (KEYNOTE) Pacific Rim International Conference on Advanced Materials and Processing (PRICM-8), Waikoloa, HI, August 2013.
24. A. D. Stiff-Roberts, "RIR-MAPLE Deposition of Organic Thin Films for Photonics and Optoelectronics," (INVITED) 139th OMICS Group International Conference and Exhibition on Lasers, Optics & Photonics, San Antonio, TX, October 2013.
25. A. Atewologun, X. Xu, and A. D. Stiff-Roberts, "Semi-Empirical Monte Carlo Model of Organic Photovoltaic Device Performance for Different Film Morphologies Deposited by RIR-MAPLE," Materials Research Society Fall Meeting, Boston, MA, December 2013 (poster).
26. W. Ge and A. D. Stiff-Roberts, "Hybrid Organic/Inorganic Solar Cells Fabricated by Resonant Infrared Matrix-Assisted Pulsed Laser Evaporation (RIR-MAPLE): Target Chemistry, Film Morphology and Device Performance," Materials Research Society Fall Meeting, Boston, CA, December 2013 (poster).
27. A. D. Stiff-Roberts, "Emulsion-Based Resonant Infrared Matrix-Assisted Pulsed Laser Evaporation: An Enabling Technology for Organic Thin Films," National Institute of Standards and Technology (NIST), Gaithersburg, MD, January 2014.
28. A. D. Stiff-Roberts, R. D. McCormick, and A. Atewologun, "Impact of Resonant Infrared Matrix-Assisted Pulsed Laser Evaporation (RIR-MAPLE) on Morphology and Charge Conduction in Conjugated Polymer and Bulk Heterojunction Thin Films," American Physical Society March Meeting, Denver, CO, March 2014.
29. A. D. Stiff-Roberts, "Resonant Infrared Matrix-Assisted Pulsed Laser Evaporation (RIR-MAPLE): An Enabling Technology for Polymeric Thin Films," American Physical Society March Meeting, Denver, CO, March 2014 (poster).
30. R. D. McCormick, W. Ge, A. Atewologun, and A. D. Stiff-Roberts, "Nanoscale Domains in Blended Organic Thin Films Deposited by RIR-MAPLE," International High-Powered Laser Ablation Conference, Santa Fe, NM, April 2014.
31. W. Y. Ge, R. D. McCormick, G. Nyikayaramba, and A. D. Stiff-Roberts, "Bulk heterojunction PCPDTBT:PC71BM organic solar cells deposited by emulsion-based, resonant infrared matrix-assisted pulsed laser evaporation," Applied Physics Letters, vol. 104, pp. 223901, June 2014.
32. W. Y. Ge and A. D. Stiff-Roberts, "The impact of emulsion preparation on organic solar cells fabricated by resonant infrared, matrix-assisted pulsed laser evaporation," Electronic Materials Conference, Santa Barbara, CA, June 2014.
33. W. Y. Ge, A. Atewologun and A. D. Stiff-Roberts, "Hybrid nanocomposite thin films deposited by emulsion-based resonant infrared matrix-assisted pulsed laser evaporation for photovoltaic application," Organic Electronics, vol. 22, pp. 98-107, March 2015.
34. A. D. Stiff-Roberts, R. D. McCormick, A. Atewologun, "Investigation of Different Organic Solar Cell Active Region Structures Deposited by Resonant Infrared

Matrix-Assisted Pulsed Laser Evaporation (RIR-MAPLE),"American Physical Society March Meeting, San Antonio, TX, March 2015.

35. A. D. Stiff-Roberts, R. D. McCormick, and W. Y. Ge, "Material properties and applications of blended organic thin films with nanoscale domains deposited by RIR-MAPLE," (INVITED) Proceedings of SPIE, vol. 9350, Laser Applications in Microelectronic and Optoelectronic Manufacturing (LAMOM) XX, pp. 935007, March 2015 (doi:10.1117/12.2079858).
36. A. D. Stiff-Roberts, "Organic and Hybrid Organic-Inorganic Thin Film Deposition by Resonant Infrared, Matrix-Assisted Pulsed Laser Evaporation," (INVITED) American Vacuum Society (AVS 62), San Jose, CA, October 2015.
37. A. D. Stiff-Roberts, W. Y. Ge, and Y. Liu, "Empirical Growth Mechanisms of Emulsion-based, Resonant Infrared, Matrix-Assisted Pulsed Laser Evaporation," Materials Research Society Fall Meeting, Boston, MA, December 2015.
38. Impact of Primary Solvent in Emulsion-Based RIR-MAPLE on Organic Solar Cell Device Performance, in preparation.